NEER FINAL REPORT

PROJECT TITLE: **ANALYTICAL RADIATION TRANSPORT BENCHMARKS FOR THE NEXT CENTURY**

AWARD NUMBER: DE-FG07-01ID14113

UNIVERSITY OF ARIZONA ACCOUNT NUMBER: 308570

PI: B.D. Ganapol
Department of Mechanical and Aerospace Engineering
University of Arizona
Ganapol@cowboy.ame.arizona.edu
Tel: 520/621-4728

DURATION: 6/4/01 to 10/30/04

ABSTRACT

Verification of large-scale computational algorithms used in nuclear engineering and radiological applications is an essential element of reliable code performance. For this reason, the development of a suite of multidimensional semi-analytical benchmarks has been undertaken to provide independent verification of proper operation of codes dealing with the transport of neutral particles. The benchmarks considered cover several one –dimensional, multidimensional, monoenergetic and multigroup, fixed source and critical transport scenarios. The first approach, called the Green's Function Method (**GFM**), features a new innovative Fourier transform solution based on an analytical moments representation of the Green's function. In slab geometry, the Green's function is incorporated into a set of integral equations for the boundary fluxes. Through a numerical Fourier transform inversion and subsequent matrix inversion for the boundary fluxes, a semi-analytical benchmark emerges. Multidimensional solutions in a variety of infinite media are also based on the slab Green's function. In a second approach, a new converged SN method is developed. In this method, the SN solution is "mined" to bring out hidden high quality solutions. For this case multigroup fixed source and criticality transport problems are considered. Remarkably accurate solutions can be obtained with this new method called the Multigroup Converged SN (MGCSN) method as will be demonstrated.

TABLE OF CONTENTS

INTRODUCTORY REMARKS

The design of nuclear reactors including the accompanying safety analyses and burnup predictions are routinely performed in today's large-scale computational environments. Methods developers have perfected computational algorithms for cross section generation, neutron transport and diffusion, and Monte Carlo calculations in order to take advantage of new computer architectures and computational algorithms that have recently emerged. As computational capacity increases with new developments in the microchip industry, ever-larger problems can be accommodated. Along with these advances in large scale computing has come an increased reliability of numerical methods and, as a result, the development of more powerful and sophisticated numerical algorithms. In particular, finite difference, finite element, nodal, PN and SN methods are among today's most effective numerical algorithms for neutron transport and diffusion theory applications. While these methods allow for consideration of comprehensive problems in nuclear engineering, they all generally possess one inherent shortcoming-- numerical discretization error. This error is a result of the finiteness, though large by past standards, of computer storage. Of course, for most algorithms, an estimate of the numerical error is provided; but usually this error is only approximate and can, under certain circumstances, be misleading. In addition, because of the mathematical and numerical complexity of the algorithms used to solve these comprehensive problems, there is always the concern that a neutron transport or diffusion algorithm has not been properly coded.

In these times of accountability and continuous improvement, it is imperative that assurance of acceptable numerical error and proper programming be provided to the customer. In order to assess the numerical error of a particular code and to address the issue of proper programming, one or all of the following tests have been routinely used in the past:

1. Observation of the conservation of quantities such as particle number, total energy and momentum
2. Comparison of results to known physical trends usually involving simplified problems with known physical behavior
3. Comparison of results with numerical algorithms designed for similar applications
4. Comparison to standards or analytical benchmarks.

It must be emphasized that there is no guaranteed method of verifying that a particular computational algorithm is performing correctly for all cases envisioned since, if there were, then there would be no need for the algorithm in the first place. The value of the tests mentioned above is in indicating algorithmic inconsistencies by their failure. Note that comparison to experiment is not included as one of the tests considered, since comparison to experiment measures how well a particular physical situation is modeled indicating nothing about the quality of the numerical results. For this reason, comparison to experiment is considered a code *validation* measure rather than code *verification* measure as will be presented here.

The primary aim of this benchmark presentation is to provide a series of analytical benchmarks to be used as standards for comparison. Currently, there is a lack of such benchmarks in the literature; and it is for this reason, that this project has been undertaken. A secondary use of these benchmarks derives from their educational value. The development of benchmarks requires a firm understanding of analytical solution techniques as well as numerical methods and computational strategies. In courses in nuclear engineering, introducing analytical benchmarks along with theory can enhance the concept of neutron interaction with matter. As will be evident, each benchmark is described in a manner that can cover a significant portion of the subject matter in the reactor theory and neutron transport theory given additional information about the physical setting and the approximations used in practice. In addition, the study of these benchmarks introduces the student to standard numerical techniques such as numerical integration and iteration strategies as well as analytical mathematical methods, error analysis and computational strategies.

1. OVERVIEW OF ANALYTICAL BENCHMARKING

When solving the neutron transport equation, a hierarchy of analytical solutions, based on accuracy, is possible. This hierarchy can be categorized as follows:

- ❑ exact-analytical
- ❑ near-analytical
- ❑ semi-analytical
- ❑ purely-numerical.

A closed form *exact-analytical* numerical solution is the ideal solution one strives toward when solving any equation. In this case, an explicit solution

representation is found in terms of elementary or special functions. The most accurate numerical evaluation of this closed form solution therefore is through infinite precision arithmetic, thus avoiding truncation error altogether. Unfortunately, the solutions to particle transport equations do not generally lend themselves to closed form representations. With the increased use of symbolic manipulation for numerical evaluation however, the ideal of the *exact-analytical* solution to the transport equation in the future is not entirely out of the question. A *near-analytical* solution to the transport equation is an evaluation of a closed form solution representation using standard numerical approximations and finite high-precision arithmetic. Such an evaluation may make use of numerical quadrature and infinite series for which error estimates are available. *Semi-analytical* solutions are finite precision numerical evaluations of a continuous variable transport solution representation that, for example, may be in the form of a set of integral equations. These solutions generally require iterative techniques with inherent error control and the potential for acceleration toward convergence. Examples of *semi-analytical* solutions are derived from integral transport theory and the 1-D Green's Function Method [Ganapol, 1999b]. Finally, the most common solutions to the transport equation involve full numerical discretization of the transport operator with respect to particle position, direction, time and energy. These *Purely numerical* solutions, while containing discretization error, are nevertheless, the most comprehensive transport solutions available and are the foundation of numerical transport applications. Algorithms such as discrete ordinates (SN formulation) can generate ultra fine mesh benchmark solutions that can be as accurate as semi-analytical benchmarks as has been demonstrated [Ganapol, 1999a].

There are several important distinctions between the classes of "analytical" (exact, near and semi) and "purely numerical" solutions. First, like numerical solutions, analytical benchmarks (with the exception of "exact") contain unavoidable numerical error resulting from finite precision arithmetic and numerical approximation. Unlike purely numerical solutions, however, the error associated with analytical benchmarks can be estimated and occurs at a level theoretically closer to the true transport solution. For this reason, analytical benchmarks provide a higher standard of quality control than purely numerical solutions. These benchmarks can effectively be used to uncover unknown numerical vagaries and coding errors, to assess the accuracy of purely numerical transport algorithms as well as to confirm proper algorithm performance. The semi-analytical benchmarks to be

developed here, therefore, can serve as convenient standards to which numerical transport algorithms for neutron transport can be compared. This is not to say that fine mesh numerical benchmarks are not as accurate as analytical benchmarks, but true confidence in their accuracy can only come from comparisons with semi-analytical benchmarks.

Because of the requirement of analytical representations, only relatively simple or idealized problems can be considered as benchmarks until the recent development of the MGCSN method (Ch. IV). For this reason, analytical benchmarks have the potential to verify only isolated segments of large comprehensive algorithms. Thus, by verification of the components of an algorithm, some confidence in the entire operation of a code can be gained. Inconsistencies and inaccuracies may still remain however because of the interfacing of components. Because of their limited nature, semi-analytical benchmarks have been criticized as being far too idealized to provide meaningful diagnostics. It must be emphasized that even though the type of problems lending themselves to analytical solutions are usually much less complicated than the comprehensive problems for which a code has originally been designed, they still have diagnostic value. *Indeed, codes required to solve the comprehensive problems must also perform well for the simple problems.*

2. BENCHMARK CLASSIFICATION

Since many benchmarks can be envisioned, a classification scheme has been established for reference purposes. Each benchmark will be classified according to the eight categories as shown in Table 1.

The first category (*C1*) specifies the type of particle considered which includes neutrons, photons, electrons, ions and molecules. In future efforts, benchmarks problems could be expanded to include all particles indicated in *C1*. Here, only neutrons will be considered in a transport setting. Category 2 (*C2*) specifies the geometry containing the field particles with which the neutrons collide. At present, one- and two- dimensional geometries will be considered. In general, the geometry can be infinite without surfaces, 1-D or 2-D half-spaces with one surface and a 1-D finite (slab) medium with two surfaces. The type of scattering kernel (isotropic, anisotropic, or general) is

Table 1 Benchmark classification

***C1*. SPECIFIC TRANSPORT FIELD**	
NT	Neutron transport
ND	Neutron diffusion
RT	Radiative transfer
EIT	Electron and ion transport
RGD	Rarefied gas dynamics
***C2*. GEOMETRY**	
P	Plane geometry (1D,2D)
SP	Spherical geometry (1D)
CY	Cylindrical geometry (1D,2D)
SPECIFIC GEOMETRY QUALIFIERS	
I	Infinite medium
H	Half-space
2H	2 half-spaces
S	Slab geometry
HE	Heterogeneous slab geometry
***C3*. ANISOTROPY OF SCATTERING KERNEL**	
I	Isotropic
LE(*L*)	Legendre expansion of order *L*
***C4*. ENERGY SPECTRUM APPROXIMATION**	
OG	One-group
MG	Multigroup
C	Continuous
***C5*. ANGULAR SOURCE DISTRIBUTION**	
I	Isotropic
B	Beam
D	Distributed
LE(*L*)	Legendre expansion of order *L*

***C6*. SPATIAL AND/OR TEMPORAL SOURCE DISTRIBUTION**	
L	Localized (delta function)
D	Distributed
PT	Pulsed in time
CT	Continuous in time
U	Uniform
***C7*. NUMERICAL TREATMENT OF INDEPENDENT VARIABLES**	
X(C,D)	Position (continuous, discrete)
A(C,D)	Angle (continuous, discrete)
T(C,D)	Time (continuous, discrete)
E(C,D)	Energy (continuous, discrete)
***C8*. NUMERICAL METHOD**	
NLTI	Numerical Laplace transform inversion
NFTI	Numerical Fourier transform inversion
FN	FN method
IT	Integral transport
VM	Variational method
RM	Reconstruction from moments
MC	Multiple collision
RR	Recurrence relation
CAC	Continuous analytical continuation
EE	Eigenfunction expansion
Other	PN, AN, etc.

specified in *C3* with the neutron energy spectrum approximation (one-group, multigroup, or continuous) given in *C4*. The angular and spatial source distributions are given in *C5* and *C6*, respectively. Information on the numerical method is specified in *C7* and *C8*, indicating which independent variables are treated either continuously (C) or discretely (D) in *C7* and the particular numerical method used in *C8*.

Each of the following four chapters represents a self contained benchmark study in which the theory is detailed and numerical results are reported. For completeness some theoretical material is repeated. The computational programs in **FORTRAN** 77 are available upon request from the PI.

REFERENCES

[**Ganapol,1999a]**, J. Warsa, J. Dahl, S. Woolf and J. Garth, *Analytical Benchmark Comparisons for Matrix Eigenvalue-, Symbolic-, p-adaptive- and Standard- S_N Formulations*, ANS Math & Comp. Topical Meeting, Madrid, 1359(1999).

[**Ganapol,1999b]**, K. Parsons, *A Heterogeneous Medium Analytical Benchmark* , ANS Math & Comp. Topical Meeting, Madrid, 456(1999).

CHAPTER I

ANALYTICAL STEADY STATE INFINITE MEDIA BENCHMARKS

1. INFINITE MEDIUM BENCHMARK DESCRIPTION

1.1. Physical Description

The most fundamental spatial configuration for the transport of neutrons is the infinite homogeneous medium. While conceptually, an infinite medium calls up a rather ordinary image of a large universe that is primarily of mathematical interest only, a closer look reveals a structure that can be useful in generating meaningful analytical transport benchmarks. An infinite medium comes in many flavors as defined by the configuration of the source emission. For instance, if the source is planar, which is an infinitesimally thin and transversely infinite plane, the variation of the resulting flux is only longitudinal (say in the *x*-direction). This is true since no surfaces or material discontinuities exist to influence particles otherwise. If the source is a point and is isotropically emitting in the same infinite medium, then the flow is radially outward giving rise to the well-known inverse *r*-squared behavior of the flux. An infinite line source also exhibits a radial flow but is uniform axially in the direction of the source. Of course, the main reason for these simple variations is that a homogeneous infinite medium has no distinguishing characteristics such as surfaces or material boundaries, other than a source position, to define a length scale. For this reason, the dimensional variation of the flux variation in an infinite medium inherits the dimensionality of the source. The flux from a plane source has variation only in the longitudinal spatial dimension; while, the flux for an isotropically emitting point source is uniform in angle at each radius. With this in mind, it is possible to define several relatively simple source configurations to provide multi-dimensional flux variations. This observation along with the analytical relations between fluxes in infinite media, allow for the development of a convenient tool to generate some rather comprehensive multidimensional analytical benchmark solutions. The generation of four simple 1-D and two 2-D benchmark solutions is the subject of this section.

1.2. Mathematical Description: NT/P:I/LE/OG/I/L/X(C),A(C)/NFTI

The theory begins with the solution of the one-group transport equation in a plane infinite medium with isotropic source emission

$$\left[\mu\frac{\partial}{\partial x}+1\right]\Psi(x,\mu)=\frac{c}{2}\sum_{l=0}^{L}\omega_l P_l(\mu)\Psi_l(x)+\frac{\delta(x)}{2}\ . \qquad (1)$$

$\Psi(x,\mu)$ represents the angular flux distribution of particles traveling in the direction μ (with respect to the *x*-axis) at the position *x* (measured in mean free paths from the source plane) and emitted by a source at *x* = 0. The Legendre moments of the scattering term in eq(1) are defined as

$$\Psi_l(x)\equiv\int_{-1}^{1}d\mu P_l(\mu)\Psi(x,\mu)$$

and the particle flux distribution is required to remain finite

$$\lim_{|x|\to\infty}\Psi(x,\mu)<\infty\ .$$

Note that any order of anisotropy *L* is allowed and the number of secondaries is *c*. If eq(1) is operated on by a Fourier transform, there results

$$(1+ik\mu)\overline{\Psi}(k,\mu)=\frac{c}{2}\sum_{l=0}^{L}\omega_l P_l(\mu)\overline{\Psi}(k)+\frac{1}{2} \qquad (2)$$

where the Fourier transform of the angular flux is

$$\overline{\Psi}(k,\mu)\equiv\int_{-\infty}^{\infty}dx\,e^{-ikx}\Psi(x,\mu)\ ;$$

and for the scalar flux

$$\overline{\Psi}(k)\equiv\int_{-\infty}^{\infty}dx\,e^{-ikx}\Psi(x)\ .$$

The scalar flux solution, which is of primary interest, is therefore the inversion

$$\Psi(x)\equiv\frac{1}{2\pi}\int_{-\infty}^{\infty}dk\,e^{ikx}\overline{\Psi}_0(k)\ .$$

Manipulation of eq(2) yields the following set of equations for the transformed moments $\overline{\Psi}_l$:

$$\sum_{l=0}^{L}\left[\delta_{jl}-c\omega_l L_{jl}(k)\right]\overline{\Psi}_l(k)=(-1)^j zQ_j(z) \qquad (3)$$

for $0\le j\le L$ where

$$L_{jl}(k)=\frac{1}{2}\int_{-1}^{1}d\mu\frac{P_j(\mu)P_l(\mu)}{1+ik\mu}\ ,$$

$$z\equiv 1/ik\ .$$

and $Q_j(z)$ is the j-th order Legendre function of the second kind. By projecting eq(2) over Legendre polynomials, a recurrence relation for the same transformed moments can also be obtained

$$zh_l\overline{\Psi}_l(k)+(l+1)\overline{\Psi}_{l+1}(k)+l\overline{\Psi}_{l-1}(k)=z\delta_{l0} \qquad (4)$$

with

$$h_l \equiv 2l+1-c\omega_l \ .$$

The set of equations most conveniently solved, however, is neither eq(3) nor eq(4) alone but a combination of both, i.e., eq(3) with $j = 0$ and eq(4) for $l = 0,\ldots L\text{-}1$.

The solution for the moments proceeds as follows. For convenience define

$$\overline{\Psi}_l(k) \equiv \overline{\Psi}_l(-z)$$

to indicate the true dependence of $\overline{\Psi}_l$. Equation (4) can therefore be written as(Ganapol,2000)

$$-zh_l\overline{\Psi}_l(z)+(l+1)\overline{\Psi}_{l+1}(z)+l\overline{\Psi}_{l-1}(z)=-z\delta_{l0} \ . \qquad (5)$$

Without loss of generality let its solution be of the form

$$\overline{\Psi}_l(z)=g_l(z)H(z)-\rho_l(z) \qquad (6)$$

where g_l is the Chandrasekhar polynomial of the first kind that satisfies the homogeneous form of eq(5). H and ρ_l are to be determined to satisfy eqs(5) and (3) for $j = 0$. Furthermore, if we impose the condition

$$H(z)=\overline{\Psi}_0(z) \ ,$$

then when eq(6) is introduced into eq(5) ρ_l must satisfy

$$-zh_l\rho_l(z)+(l+1)\rho_{l+1}(z)+l\rho_{l-1}(z)=0 \ . \qquad (7)$$

with starting value

$$\rho_0(z)\equiv 0 \ .$$

Equation (7) defines the ρ_l-polynomials, called the Chandrasekhar polynomials of the second kind. $\overline{\Psi}_0(z)$ is found by substitution of eq(6) into eq(3) with $j = 0$ to give

$$\overline{\Psi}_0(k)=\frac{\tilde{g}_L(k)}{\Lambda_L(k)} \ , \qquad (8a)$$

where

$$\Lambda_L(k)=1-cz\sum_{l=0}^{L}\omega_l Q_l(z)g_l(z) \qquad (8b)$$

and

$$\tilde{g}_L(k)=\tilde{g}_L(z)\equiv zQ_0(z)-cz\sum_{l=0}^{L}\omega_l Q_l(z)\rho_l(z). \qquad (8c)$$

$\Lambda_L(z)$ is recognized as the usual dispersion relation for anisotropic scattering defined in terms of Chandrasekhar polynomials of the first kind. Once this connection has been established, the simplifying relations of Inonu [Inonu,1973] can be used to give the remarkably compact representation

$$\Lambda_L(z)=(L+1)\left[g_{L+1}(z)Q_L(z)-g_L(z)Q_{L+1}(z)\right] \ . \qquad (9)$$

Apparently, the role of the ρ_l-polynomials is to define the numerator $\tilde{g}_L(k)$ of the zeroth moment transform of the. Following the same procedure (see Appendix A) as Inonu's, but for the ρ_l-polynomials, gives the corresponding condensed relation

$$\tilde{g}_L(z) = (L+1)\left[\rho_{L+1}(z)Q_L(z) - \rho_L(z)Q_{L+1}(z)\right] \tag{10}$$

and eq(8a) becomes

$$\overline{\Psi}_0(k) = \left[\frac{\rho_{L+1}(z)Q_L(z) - \rho_L(z)Q_{L+1}(z)}{g_{L+1}(z)Q_L(z) - g_L(z)Q_{L+1}(z)}\right] . \tag{11}$$

The scalar flux in plane geometry is therefore obtained from the following Fourier transform inversion:

$$\Psi(x) \equiv \frac{1}{2\pi}\int_{-\infty}^{\infty} dk\, e^{ikx}\left[\frac{\tilde{g}_L(k)}{\Lambda_L(k)}\right] . \tag{12}$$

This inversion can be evaluated either by analytical continuation of the integrand to pick up contributions from the poles (zeros of the dispersion relation) and branch cuts $\{[\pm i, \pm i\infty)\}$ or by numerical evaluation of the inversion integral directly. The latter is the evaluation of choice since it avoids determining the zeros of the dispersion explicitly.

1.3. Additional 1-D Sources

With the explicit representation of the scalar flux in a plane infinite medium known, it is now possible to define flux variations for sources in other more complex and realistic infinite media settings.

A. Point source: NT/SP:I/LE/OG/I/L/X(C),A(C)/NFTI

The flux from a point source is simply obtained from the plane/point transformation [Case, 1967]

$$\Phi_{pt}(r) = -\frac{1}{2\pi r}\frac{d\Psi(r)}{dr}$$

which gives from eq(12)

$$\Phi_{pt}(r) \equiv \frac{1}{2\pi}\int_{-\infty}^{\infty} dk\, e^{ikr}\left[\frac{\tilde{g}_L(k)}{z\Lambda_L(k)}\right] . \tag{13}$$

B. Shell source: NT/SP:I/LE/OG/I/L/X(C),A(C)/NFTI

The point source flux can then be used to give the flux from a shell source of radius *a*. If a point source is integrated over the shell of as shown

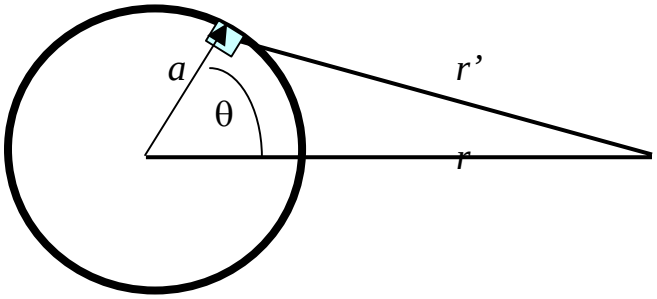

the flux at r is

$$\Phi_{sh}(r,a) = q_0 \frac{a}{r}\left[\Phi_{pl}(|r-a|) - \Phi_{pl}(r+a)\right] . \qquad (14a)$$

For a normalization of one particle emitted over the entire shell area

$$q_0 = \frac{1}{4\pi a^2} ,$$

we have

$$\Phi_{sh}(r,a) = \frac{1}{4\pi a r}\left[\Phi_{pl}(|r-a|) - \Phi_{pl}(r+a)\right] . \qquad (14b)$$

C. Solid spherical source: NT/SP:I/LE/OG/I/L/X(C),A(C)/NFTI

The flux form a spherical shell source of radius r_0 is obtained by integration of the shell source over the spherical source volume

$$\Phi_{sp}(r) = q_0 \int_0^{r_0} da\, \Phi_{sh}(r,a) .$$

When eq(14a) is substituted into this expression, there results

$$\Phi_{sp}(r) = \frac{1}{4\pi r_0^3 r}\int_{-r_0}^{r_0} da\, a\Phi_{pl}(|r-a|) \qquad (15)$$

where the normalization

$$q_0 \equiv \frac{1}{4\pi r_0^3}$$

has been defined along with a change of variable to condense the integration. When eq(12) is introduced into eq(15) and the integration order interchanged, the final expression becomes

$$\Phi_{sp}(r) = \frac{1}{\pi}\int_{-\infty}^{\infty} dk e^{ikr}\left\{ z\frac{\tilde{g}_L(k)}{\Lambda_L(k)}\left[\frac{\sin(kr_0)}{k} - r_0\cos(kr_0)\right]\right\} . \qquad (16)$$

1.4. 2-D Sources

The advantage of the Fourier transform approach is that multi-dimensional source can be constructed as will be demonstrated in this section.

A. Finite line source: NT/CY:I/LE/OG/I/L/X(C),A(C)/NFTI

The flux at the position (ρ, z) from the finite line source shown is

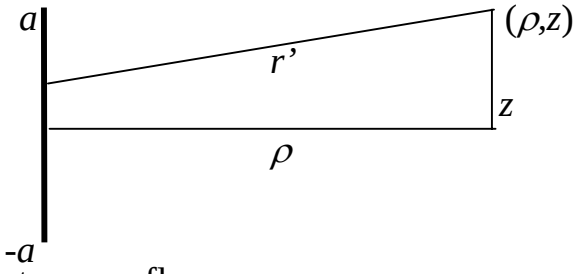

given by an integration of the point source flux

$$\Phi_{2Dl}(\rho,z)=\int_{-a}^{a}dz'\Phi_{pt}(r')$$

which becomes through a change of variable

$$\Phi_{2Dl}(\rho,z)=\frac{1}{2}\int_0^1 d\omega\left[\Phi_{pt}\left(\sqrt{\rho^2+(z-a\omega)^2}\right)+\Phi_{pt}\left(\sqrt{\rho^2+(z+a\omega)^2}\right)\right]. \quad (17)$$

For this case, the normalization is the inverse of the line source length. Unlike the 1-D sources, one additional integration is required. The integration in eq(17) will be performed by Gauss/Legendre quadrature to a high degree of accuracy as discussed below.

B. Ring source: NT/CY:I/LE/OG/I/L/X(C),A(C)/NFTI

In a similar fashion, the flux from the circular source shown is found

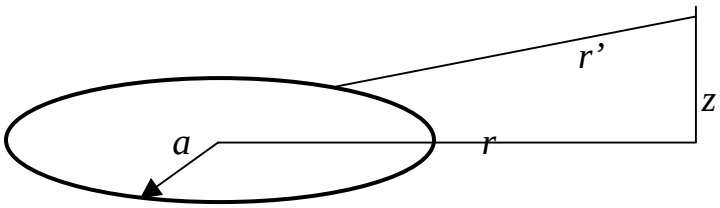

to be

$$\Phi_{Cr}(\rho,z)=\frac{1}{\pi}\int_0^{\pi}d\theta\,\Phi_{pt}\left(\sqrt{z^2+a^2+r^2-2ar\cos(\theta)}\right). \quad (18)$$

where the normalization

$$q_0\equiv\frac{1}{2\pi a}$$

was used. Again the integration will be performed numerically.

1.5. Numerical Implementation

A. Numerical Fourier transform inversion

The primary numerical procedure required for the numerical implementation of the six sources described above is the numerical Fourier transform

inversion. This algorithm has been described in a previous report [Ganapol,1991] and therefore will not be described further other than to say it is an efficient and accurate algorithm for the inversions of the image functions presented above.

Because of the singular nature of the flux from both the plane and point sources, the most appropriate representations of the solutions are

$$\Psi(x) \equiv \frac{1}{2} E_1(x) + \frac{1}{2\pi} \int_{-\infty}^{\infty} dk\, e^{ikx} \left[\frac{\tilde{g}_L(k)}{\Lambda_L(k)} - zQ_0(z) \right] \tag{19a}$$

$$\Phi_{pt}(r) \equiv \frac{e^{-r}}{4\pi r^2} + \frac{1}{2\pi} \int_{-\infty}^{\infty} dk\, e^{ikr} \left[\frac{\tilde{g}_L(k)}{z\Lambda_L(k)} - Q_0(z) \right] \tag{19b}$$

where the uncollided fluxes have been explicitly computed. Note that E_1 is the exponential integral. In this way, the singularities are isolated in the leading terms allowing the inversions to be determined more accurately.

B. Additional integration for 2-D sources

The addition integrations in eqs(17) and (18) are performed using Gauss/Legendre (GL) integration of order **Lm** shifted to the appropriate intervals. To expedite the integration and with an eye to accommodation of 3-D sources, an interpolation assisted integration scheme has been devised. Since these integrations involve only the point flux, rather than evaluate this flux at all the integration abcissae, a simple interpolation scheme can be employed. This is possible since the integrand depends only on the distance from a point on the source to the point where the flux is to be found. By predetermining the range of these distances (nearest to farthest) for all edit points, Φ_{pt} can be calculated at **nb** points in-between. Thus, the desired integration abcissae can be obtained from (polynomial) interpolation. This procedure greatly reduces the computational effort but may not guarantee benchmark accuracy unless iteration on **nb** is required as to be discussed.

C. Iteration on quadrature order and interpolation abcissae

In order to guarantee benchmark quality results, an outer iteration on the quadrature order (**Lm**) and the number of interpolation abcissae (**nb**) has be instituted. For simplicity, **Lm** and **nb** are set equal and the iteration counter applies to both. These quantities are increased by two until the fluxes converge on the edit grid or the maximum number of iterations is reached. While benchmark accuracy (4- or 5- places) can be useful for 1-D problems, most likely this will not be necessary for multi-dimensional comparisons

since not more than three (or at most four digits) are expected from a 2- or 3-D numerical transport algorithm.

2. Program Notes and Desired Results

A **FORTRAN** 77 program called **TIELV1.f** has been written to implement the numerical evaluation of the flux for the sources described above. The program input and a sample problem are found in Appendix B. Multiple cases can be accommodated with output from 1-D sources appropriate for (SigmaPlot™) plotting written to file **plt1.dat** and for 2-D sources written to file **plt2.dat** (2-D) or **plt3.dat** (3-D).

For best results and ease of use, the following considerations need to be taken into account when running **TIELV1.f**:

1) The differential scattering cross section can be
   + read in from supplied file **wl.dat**
   + Henyey-Greenstein ($\omega_l = g^l$)
   + screened –Rutherford kernel
   + elastic scattering kernel.

2) Because the integrands in eqs(17) and (18) become more singular on approach to either the line or circular sources, the integration will eventually fail. This breakdown occurs because the flux approaches infinity on approach to either of these sources. For this reason, best results are obtained for edit points at least 0.05 mfp from the sources.

3) For multiple cases, all cases will have the same spatial edit grid.

4) The flux within a solid sphere is not determined and is therefore set to zero.

5) The flux from a spherical source can be evaluated by both the direct (**isrc** = 4) and assisted (**isrc** = 41) integration schemes.

The results of the first demonstration are given in Table 1. This demonstration considers the appropriateness of assisted (interpolated) integration versus direct integration for a spherical source of radius $r_0 = 1$. Four cases were run with the first three cases using direct integration with increasing quadrature order from 10 to 50 and the last case for assisted integration of order 50. As can be observed, the direct and assisted integration schemes do indeed converge.

Table 1
Demo 1: 1-D Spherical Source for the Two Integration Schemes
[H-G:g = 0.95 L = 20 c = 0.99]

r\Lm(ISRC)	10(41)	25(41)	50(41)	50(4)
1.0000E+00	1.1155E-01	1.2147E-01	1.215**6**E-01	1.2159E-01
1.1000E+00	7.8594E-02	8.6607E-02	8.661**5**E-02	8.6614E-02
1.2000E+00	6.2022E-02	6.8673E-02	6.8683E-02	6.8683E-02
1.3000E+00	5.1197E-02	5.6512E-02	5.652**3**E-02	5.6522E-02
1.4000E+00	4.3598E-02	4.7610E-02	4.7620E-02	4.7620E-02
1.5000E+00	3.8091E-02	4.0802E-02	4.0813E-02	4.0813E-02
1.6000E+00	3.4008E-02	3.5438E-02	3.5449E-02	3.5449E-02
1.7000E+00	3.0959E-02	3.1118E-02	3.1129E-02	3.1129E-02
1.8000E+00	2.8625E-02	2.7576E-02	2.7587E-02	2.7587E-02
1.9000E+00	2.6771E-02	2.4628E-02	2.4640E-02	2.4640E-02
2.0000E+00	2.5135E-02	2.2147E-02	2.2159E-02	2.2159E-02

The results for demonstrations 2 and 3 are shown in Figs. 1 and 2. In Fig. 1, the flux variation for the four 1-D sources is shown. The distinct nature of each source is clearly evident. As the distance from the sources increases however, the fluxes for the spherical geometries merge. The flux from the plane source remains different because of its transversely infinite extent. Figure 2 shows the 2-D flux from the upper half of line source. Near the source, the flux clearly outlines the (upper half) source extent with a gradual loss of spatial detail with distance from the source.

REFERENCES

[**Case, 1967**], and P. Zweifel, *Linear Transport Theory*, Addison Wesley, MA, (1967).

[Ganapol,1991], INEL Report, EGG-NE-9641, 4/9,1991.

[Ganapol,2000], *A Consistent Theory of Neutral Particle Transport in an Infinite Medium*, TTSP, 43(2000)

[**Inonu,1973**], E. Inonu, *Jour. Math. Phys*., V11, 568(1973).

Appendix A
An Alternative Representation for $\tilde{g}_L(z)$

Following the procedure as outlined by Inonu [1], we begin with the recurrence relation for $\rho_j(z)$

$$-zh_j\rho_j(z)+(j+1)\rho_{j+1}(z)+j\rho_{j-1}(z)=0 \ .$$

When this relation is multiplied by $Q_j(z)$ and summed from j=1 to L, there results

$$(L+1)\left[\rho_{L+1}(z)Q_L(z)-\rho_L(z)Q_{L+1}(z)\right]+$$
$$+\sum_{j=1}^{L}\rho_j(z)\left\{jQ_{j-1}(z)-(2j+1)zQ_j(z)+(j+1)Q_{j+1}(z)\right\}=zQ_0(z)-\omega z\sum_{j=0}^{L}\omega_j\rho_j(z)Q_j(z).$$

The term in curly brackets vanishes since it is the recurrence relation for $Q_j(z)$ and the RHS is $\tilde{g}_L(z)$ giving the simplified expression

$$\begin{aligned}\tilde{g}_L(z) &= zQ_0(z)-\omega z\sum_{l=0}^{L}\omega_l\rho_l(z)Q_l(z)\\ &= (L+1)\left[\rho_{L+1}(z)Q_L(z)-\rho_L(z)Q_{L+1}(z)\right]. \qquad \text{(A1)}\end{aligned}$$

Appendix B

Sample Problem Input and Output

The input description to **TIELV1** is given below. Also included is

Table B.1

Input Description

```
c input description (file tielv1.dat)*********************************
c line 0 case identification
c
c line 1 ncc    number of cases
c        lmt    number of quadrature order iterations (10)
c
c line 2 nx     number of edit intervals between x0 and xl
c        x0     initial edit point
c        xl     final edit point
c
c note:if line 3 is not needed,enter one blank line
c line 3 mz     number of z edit points (for isrc=5,6 only)
c        z0     initial z edit point
c        zl     final z edit point
c
c note: repeat for each of the ncc cases
c line 4 iwl    1 read scattering coefficients (wl) from wl.dat file
c               2 Henyey-Greenstein (H-G) kernel
c               3 screened-Rutherford kernel
c               4 neutron elastic scattering
c        (note:if iwl<0 use transport correction)
c        ga     g fo H-G and atomic mass for elastic neutron scattering
c        llmx   scattering order
c        w      number of secondaries
c        a0     shell,sphere radius or half line length
c        isrc   1  plane source
c               2  point source
c               3  shell source
c               4  spherical source (by direct inversion)
c               41 spherical source (by numerical integration)
c               5  line source
c               6  circular source
c        mb0    initial quadrature order (20)
c        err    desired relative error (1.0e-04)
c ****************************************************************
```

input and output for a sample problem. The sample problem is for H-G

Table B.2
Sample Problem Input

```
sample problem
4 5                                  /ncc,lmt
10 0.01 4.0                         /nx,x0,xl
2 0.1 10.0                         /mx
2 0.95 10 0.9 1.0 3 20 1.0e-04 /iwl,ga,llmx,w,r0,isrc,mb,err
2 0.95 15 0.9 1.0 3 20 1.0e-04 /iwl,ga,llmx,w,r0,isrc,mb,err
2 0.95 20 0.9 1.0 3 20 1.0e-04 /iwl,ga,llmx,w,r0,isrc,mb,err
2 0.95 25 0.9 1.0 3 20 1.0e-04 /iwl,ga,llmx,w,r0,isrc,mb,err
```

Table B.3
Sample Problem Screen Output

```
begin case  1
   iwl    ga     llmx     w         a0     isrc mb     err
    2  9.500E-01  10  9.000E-01  1.000E+00   3  20  1.000E-04
 quadrature order = 20 error=  0.000E+00
 quadrature order = 22 error=  1.268E-04
 quadrature order = 24 error=  6.560E-05
 begin case  2
    2  9.500E-01  15  9.000E-01  1.000E+00   3  20  1.000E-04
 quadrature order = 20 error=  0.000E+00
 quadrature order = 22 error=  1.248E-04
 quadrature order = 24 error=  6.456E-05
 begin case  3
    2  9.500E-01  20  9.000E-01  1.000E+00   3  20  1.000E-04
 quadrature order = 20 error=  0.000E+00
 quadrature order = 22 error=  1.252E-04
 quadrature order = 24 error=  6.467E-05
 begin case  4
    2  9.500E-01  25  9.000E-01  1.000E+00   3  20  1.000E-04
 quadrature order = 20 error=  0.000E+00
 quadrature order = 22 error=  1.252E-04
 quadrature order = 24 error=  6.473E-05


 1-d Sources
    x/case          1           2           3           4
    error=      6.5601E-05   6.4563E-05   6.4666E-05   6.4728E-05
   1.0000E-02   7.3027E-02   7.4197E-02   7.4012E-02   7.3992E-02
   4.0900E-01   7.8143E-02   7.9200E-02   7.8923E-02   7.8943E-02
   8.0800E-01   1.0533E-01   1.0499E-01   1.0476E-01   1.0492E-01
   1.2070E+00   7.3611E-02   7.3498E-02   7.3328E-02   7.3433E-02
   1.6060E+00   3.2381E-02   3.2708E-02   3.2649E-02   3.2652E-02
   2.0050E+00   1.8808E-02   1.8942E-02   1.8942E-02   1.8939E-02
   2.4040E+00   1.2284E-02   1.2322E-02   1.2327E-02   1.2326E-02
   2.8030E+00   8.5925E-03   8.5956E-03   8.5984E-03   8.5984E-03
   3.2020E+00   6.2931E-03   6.2870E-03   6.2879E-03   6.2880E-03
   3.6010E+00   4.7667E-03   4.7599E-03   4.7600E-03   4.7601E-03
   4.0000E+00   3.7052E-03   3.7001E-03   3.7000E-03   3.7000E-03

 plot file plt1.dat:1-D sources
```

scattering for g=0.95 in a medium with c = 0.9 and for a shell source of radius 1. The scattering order L was increased from 10 to 25 in increments of 5. The input on file **tielv1.dat** is given in Table B.2 and the screen output in Table B.3. Line 4 for each case is written followed by a convergence history as the quadrature order is increased from **Lm** = 20. Each case is displayed in a column with the first line indicating the last estimated relative error converged or not. The file **plt1.dat** is also written for plotting or to be a table.

The convergence in scattering order is clearly observed. As expected, the convergence is better further from the source. The convergence in scattering order will be the subject of a future research effort.

Fig. 1 Demo 2: 1-D sources
[H-G:g = 0.9 L = 20 c = 0.9]

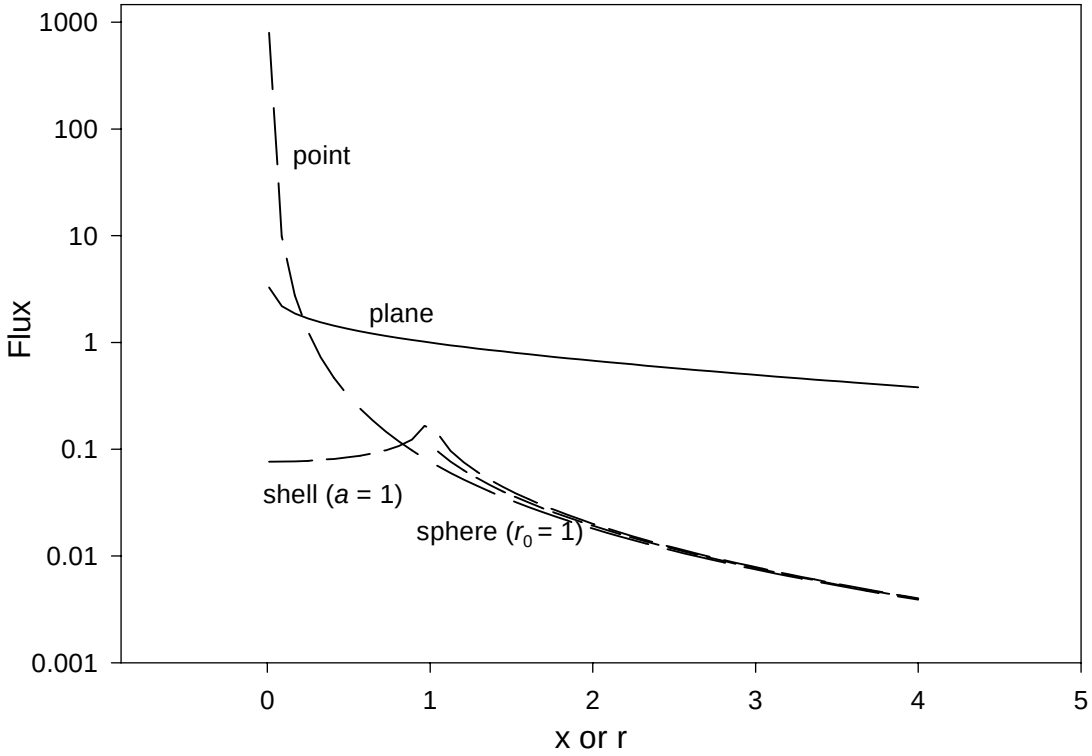

Fig. 2 Demo 3: 2-D Line Source
[H-G:g = 0.9 L = 20 c = 0.9 a = 1.0]

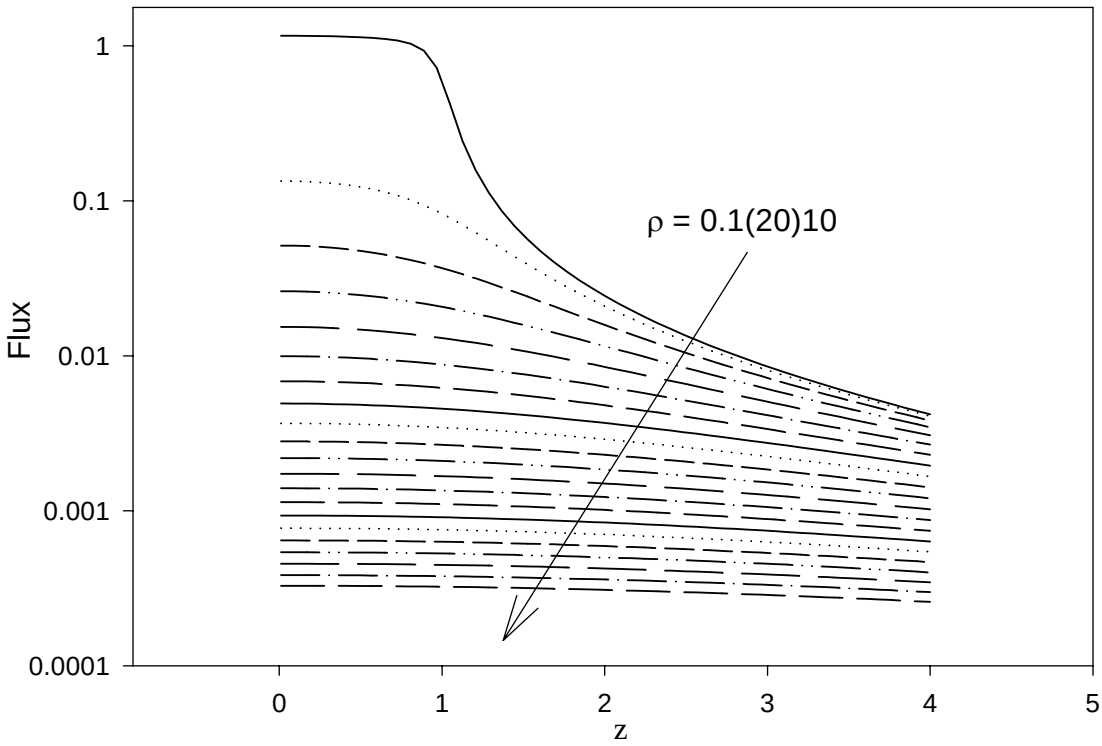

CHAPTER II

MULTIGROUP NEUTRAL PARTICLE TRANSPORT THEORY

1. INTRODUCTION

In the past, considerable attention was given to demonstrating that a theory of singular eigenfunctions existed for the solution to the multigroup transport equation [1-6]. This activity was a natural outgrowth of the many investigations concerning the one-group case that had been so elegantly treated by Case and Zweifel [7]. Some of the earliest considerations relied on knowledge of the solution form before attempting a theory. In other words, the form of the singular eigenfunction solution had to be guessed. In reviewing early attempts to develop a full-range multigroup singular eigenfunction expansion for general anisotropic scattering, the achievements, at best, were rather disappointing. No explicit theory had been put forth until 1976 when, in a seminal work, the Larsen-Habetler technique was applied to the multigroup case with isotropic scattering[8,9]. Anisotropic scattering was not treated however. The primary motivation for this chapter is to show that a multigroup full-range expansion can indeed be obtained for the partial Green's function in plane geometry from the Fourier transform approach. The curiosity here is that the solution can be found without resorting to the relatively obscure mathematics associated with singular eigenfunctions and resolvant operators. In addition, the Fourier transform approach yields a convenient expression of the solution suitable for numerical evaluation in a variety of geometrical settings as will be demonstrated.

A firmly established Fourier transform theory, paralleling that of the one-group case, will be presented for an isotropically emitting source in the multigroup plane geometry approximation. Then by using the resulting image function in a numerical Fourier transform inversion, analytical benchmark quality scalar fluxes will be obtained in both plane and spherical geometries.

In one-group transport theory, it is well known that the solution to the transport equation in an infinite medium obtained via singular eigenfunctions and from Fourier transforms are identical for isotropic scattering. When higher order scattering is considered, the correspondence

was not at all apparent until recently [10,12]. In reference 10, it was shown that the Fourier transform image function leads to the singular eigenfunction solution when analytically continued into the complex plane even for general anisotropic scattering. It is the intent of this presentation to apply similar reasoning to the multigroup case (limited to isotropic source emission) in order to extend the fundamental theoretical development of linear transport theory and partially "close the loop". In the process, as in Ref. 10, an image function appropriate for numerical inversion is obtained allowing for an accurate numerical evaluation of the partial Green's function in plane and associated geometries.

2. FOURIER TRANSFORM SOLUTION

We begin with the following special form of the multigroup transport equation for the partial Green's function in an infinite medium (isotropic source emission):

$$\left[\mu \underline{I}\frac{\partial}{\partial x}+\underline{\Sigma}\right]\vec{\Psi}(x,\mu)=\frac{1}{2}\sum_{l=0}^{L}P_l(\mu)\underline{C}_l\vec{\Psi}_l(x)+\frac{1}{2}\delta(x)\vec{q} \quad (1a)$$

for G groups. The Legendre moment vectors are defined as

$$\vec{\Psi}_l(x)\equiv\int_{-1}^{1}d\mu P_l(\mu)\vec{\Psi}(x,\mu), \quad (1b)$$

and the boundary condition is

$$\lim_{|x|\to\infty}\vec{\Psi}(x,\mu)<\infty \ . \quad (1c)$$

The group-to-group transfer matrix is $\underline{C}_l$ and the source vector $\vec{q}$ can include sources in all G groups

$$\vec{q}\equiv\left[q_1,q_2,...,q_G\right]^T \ .$$

An underbar, i.e., $\underline{M}$, indicates a matrix quantity. $\vec{\Psi}(x,\mu)$ is the G-component angular flux vector; and for theoretical convenience, the G-group parameters have been normalized such that the original total cross section of group g (s_g) is expressed as

$$\sigma_g \equiv s_g / s_{min} \geq 1$$
$$s_{min} \equiv \min_{1 \leq g \leq G} \left(s_g \right)$$

with the total cross section matrix represented by

$$\underline{\Sigma} \equiv diag\left[\sigma_g\right] .$$

The Legendre scattering coefficients have also been appropriately modified. In addition, the spatial coordinate has been changed to the dimensionless coordinate

$$x \rightarrow x\, s_{min} \ .$$

Eq(1a) can be recast into the fundamental matrix form

$$\left[\mu \underline{I} \frac{\partial}{\partial x} + \underline{\Sigma} \right] \underline{\Psi}(x,\mu) = \frac{1}{2} \sum_{l=0}^{L} P_l(\mu) \underline{C}_l \underline{\Psi}_l(x) + \frac{1}{2} \delta(x) \underline{I} \quad (2a)$$

where

$$\vec{\Psi}(x,\mu) = \underline{\Psi}(x,\mu)\, \vec{q} \quad (2b)$$

and now $\underline{\Psi}(x,\mu)$ is the matrix solution. With the application of the Fourier transform,

$$\underline{\Psi}(k,\mu) \equiv \int_{-\infty}^{\infty} dx\, e^{ikx}\, \underline{\Psi}(x,\mu) \ , \quad (3)$$

eq(2a) can algebraically be solved to give

$$\underline{\Psi}(k,\mu) = \frac{1}{2} \left[\underline{\Sigma} - ik\mu \underline{I}\right]^{-1} \sum_{l=0}^{L} P_l(\mu) \underline{C}_l \underline{\Psi}_l(k) + \frac{1}{2} \left[\underline{\Sigma} - ik\mu \underline{I}\right]^{-1} . \quad (4)$$

In the following, a function of *k* or *z* will denote a Fourier transform.

The representation of the transformed angular flux given by eq (4) is central to the analysis to follow. It will subsequently be shown that the Fourier transform inversion

$$\underline{\Psi}(x,\mu) \equiv \frac{1}{2\pi}\int_{-\infty}^{\infty} dk\, e^{-ikx}\,\underline{\Psi}(k,\mu) \ , \qquad (5)$$

leads to the singular eigenfunction expansion. The approach taken is to specify the moments $\underline{\Psi}_l$ used to reconstruct $\underline{\Psi}$ from its Legendre polynomial expansion.

In the usual way, projection over Legendre polynomials on the interval [-1,1] gives a set of moment equations

$$\underline{\Psi}_j(k) = z\sum_{l=0}^{L} \underline{V}_{jl}(z\underline{\Sigma})\underline{C}_l\underline{\Psi}_l(k) + z\ \underline{V}_{j0}(z\underline{\Sigma}) \qquad (6a)$$

where

$$\underline{V}_{jl}(z\underline{\Sigma}) = \underline{V}_{lj}(z\underline{\Sigma}) \equiv \frac{1}{2}\int_{-1}^{1} d\mu P_j(\mu)P_l(\mu)\underline{D}(z,\mu) \qquad (6b)$$

with

$$\underline{D}(z,\mu) \equiv [z\underline{\Sigma} - \mu\underline{I}]^{-1} \ .$$

Also, the new independent variable z has been defined as

$$z \equiv 1/ik$$

giving the true functional relation of the solution to eq(6a) as

$$\underline{\Psi}_l(k) \equiv \underline{\Psi}_l(z) \ .$$

Note that the (diagonal) matrix Legendre function of the second kind is defined by

$$\begin{aligned}\underline{Q}_l(z\underline{\Sigma}) \equiv \underline{V}_{0l}(z\underline{\Sigma}) &= diag\left[Q_l(z\sigma_1),...,Q_l(z\sigma_G)\right] \\ &= diag\left[\frac{1}{2}\int_{-1}^{1} d\mu \frac{P_l(\mu)}{z\sigma_g - \mu}\right].\end{aligned} \qquad (7)$$

The matrix inversion of eq(6a), in essence, provides the desired moment transforms; but essential features of the solution are hidden in so doing. For this reason, only the specific case, $j = 0$ is considered

$$\underline{\Psi}_0(z) = z \sum_{l=0}^{L} \underline{Q}_l(z\underline{\Sigma})\underline{C}_l \underline{\Psi}_l(z) + z\underline{Q}_0(z\underline{\Sigma}) \qquad (8)$$

coupled with moment equations. The last equation can be written more concisely as

$$\sum_{l=0}^{L}\left[\delta_{l,0}\underline{I} - z\underline{Q}_l(z\underline{\Sigma})\underline{C}_l\right]\underline{\Psi}_l(z) = z\,\underline{Q}_0(z\underline{\Sigma})\ . \qquad (9)$$

A set of moment equations is obtained by projection of eq(2a) over

$$[z\underline{\Sigma} - \mu\underline{I}]P_j(\mu)$$

on the interval [-1,1]. In the usual way, from the well known recurrence relation for Legendre polynomials

$$(2l+1)\mu P_l(\mu) = (l+1)P_{l+1}(\mu) + lP_{l-1}(\mu), \qquad (10)$$

the following recurrence relation for the moments results for $0 \le l \le L$:

$$-z\underline{h}_l\underline{\Psi}_l(z) + (l+1)\underline{\Psi}_{l+1}(z) + l\underline{\Psi}_{l-1}(z) = -(2l+1)z\delta_{l.0} \qquad (11a)$$

where

$$\underline{h}_l \equiv (2l+1)\underline{\Sigma} - \underline{C}_l\ . \qquad (11b)$$

The general, solution to this recurrence relation can be formulated as

$$\underline{\Psi}_l(z) = \underline{G}_l(z)\underline{\Psi}_0(z) - \underline{\rho}_l(z) \qquad (12)$$

where the matrix *G*-and ρ- polynomials satisfying

$$\begin{gathered} -z\underline{h}_l\underline{G}_l(z) + (l+1)\underline{G}_{l+1}(z) + l\underline{G}_{l-1}(z) = 0 \\ \underline{G}_0(z) \equiv \underline{I} \end{gathered} \qquad (13a)$$

$$-z\underline{h}_l\underline{\rho}_l(z)+(l+1)\underline{\rho}_{l+1}(z)+l\underline{\rho}_{l-1}(z)=z\delta_{l0}\underline{I}$$
$$\underline{\rho}_0(z)\equiv\underline{0} \qquad \text{(13b)}$$

have been introduced. It should be noted that an entirely parallel procedure to the one-group case is being followed here. $\underline{\Psi}_0(z)$ is obtained by substitution of the moment representation of eq(12) into eq(9) to give

$$\underline{\Psi}_0(z)=\underline{\Lambda}_L^{-1}(z)\hat{\underline{g}}_L(z) \qquad \text{(14a)}$$

or more explicitly

$$\underline{\Psi}_0(z)=\left[\underline{Q}_L(z\underline{\Sigma})\underline{G}_{L+1}(z)-\underline{Q}_{L+1}(z\underline{\Sigma})\underline{G}_L(z)\right]^{-1}\bullet$$
$$\bullet\left[\underline{Q}_L(z\underline{\Sigma})\underline{\rho}_{L+1}(z)-\underline{Q}_{L+1}(z\underline{\Sigma})\underline{\rho}_L(z)\right]. \qquad \text{(14b)}$$

To obtain eq(14b), the recurrence relation for $\underline{G}$ and $\underline{\rho}$ were used to condense the resulting expressions to those shown. Equation (14b) will serve as the kernel from which all numerical results will come.

3. SINGULAR EIGENFUNCTION SOLUTION

We now consider the homogeneous form of eq(2a)

$$\left[\mu\underline{I}\frac{\partial}{\partial x}+\underline{\Sigma}\right]\underline{\Phi}(x,\mu)=\frac{1}{2}\sum_{l=0}^{L}P_l(\mu)\underline{C}_l\underline{\Phi}_l(x)\ . \qquad \text{(15)}$$

After a Fourier transform, eq(15) becomes

$$\left[\underline{\Sigma}-ik\mu\underline{I}\right]\underline{\Phi}(z,\mu)=\frac{1}{2}\sum_{l=0}^{L}P_l(\mu)\underline{C}_l\underline{\Phi}_l(z) \qquad \text{(16)}$$

and upon projection over Legendre polynomials, we find

$$-z\underline{h}_l\underline{\Phi}_l(z)+(l+1)\underline{\Phi}_{l+1}(z)+l\underline{\Phi}_{l-1}(z)=\underline{0}\ . \qquad \text{(17)}$$

Since we began with a homogeneous equation, the normalization

$$\underline{\Phi}_l(z)\equiv\underline{I}$$

can be defined in which case it is clear that

$$\underline{\Phi}_l(z) = \underline{G}_l(z) \ . \qquad (18)$$

It is now convenient to construct the Legendre polynomial representation of $\underline{\Phi}(z,\mu)$ as

$$\underline{\Phi}(z,\mu) = \sum_{l=0}^{\infty} \left(\frac{2l+1}{2} \right) \underline{G}_l(z) P_l(\mu) \ . \qquad (19)$$

When eq(19) is introduced into the Legendre polynomial representation of $\underline{\Psi}(z,\mu)$

$$\underline{\Psi}(z,\mu) = \sum_{l=0}^{\infty} \left(\frac{2l+1}{2} \right) \underline{\Psi}_l(z) P_l(\mu) \ , \qquad (20)$$

there results

$$\underline{\Psi}(z,\mu) = \underline{\Phi}(z,\mu)\underline{\Psi}_0(z) - \underline{R}(z,\mu) \qquad (21a)$$

where

$$\underline{R}(z,\mu) \equiv \sum_{l=0}^{\infty} \left(\frac{2l+1}{2} \right) \underline{\rho}_l(z) P_l(\mu) \ . \qquad (21b)$$

It should be emphasized that both $\underline{\Phi}(z,\mu)$ and $\underline{R}(z,\mu)$ are distributions when z is taken on the real line but otherwise are analytic functions in the z-plane.

An alternative form for $\underline{\Phi}(z,\mu)$ can be obtained from the solution of eq(16), which takes some special care. In particular, the solution can be written as

$$\underline{\Phi}(z,\mu) = \frac{z}{2} [z\underline{\Sigma} - \mu \underline{I}]^{-1} \sum_{l=0}^{L} P_l(\mu) \underline{C}_l \underline{\Phi}_l(z) + \underline{\delta}(z,\mu) \underline{\Lambda}_L(z) \qquad (22a)$$

where

$$\underline{\delta}(z,\mu) \equiv \sum_{l=0}^{\infty} \left(\frac{2l+1}{2} \right) \underline{P}_l(z\underline{\Sigma}) \underline{P}_l(\mu \underline{I}) \qquad (22b)$$

with

$$\underline{P}_l(z\underline{D}) \equiv diag\left[P_l(zd_1), ..., P_l(zd_G) \right] \qquad (22c)$$

for the diagonal matrix $\underline{D}$. In addition, $\underline{P}_l(z\underline{\Sigma})$ satisfies the recurrence

$$(2l+1) z\underline{\Sigma} \underline{P}_l(z\underline{\Sigma}) = (l+1) \underline{P}_{l+1}(z\underline{\Sigma}) + l \underline{P}_{l-1}(z\underline{\Sigma}), \qquad (23)$$

and the normalization of $\underline{\Phi}(z,\mu)$ to $\underline{I}$ has been used. Note that the second term of the solution comes from the condition

$$[z\underline{\Sigma} - \mu \underline{I}] \delta(z,\mu) = 0$$

and that on the real line ($-\infty < \nu < \infty$)

$$\underline{\delta}(\nu,\mu) = diag\left[\delta(\sigma_1 \nu - \mu), \delta(\sigma_2 \nu - \mu), ... \delta(\sigma_G \nu - \mu) \right] .$$

Equation (22a) has a striking resemblance to the case eigenfunctions but is in transform space.

We are now in position to specify the Fourier inversion of eq(21a) noting that $\underline{\Phi}(z,\mu)$ is analytic [see eq(19)] and $\underline{\Psi}_0(z)$ is sectionally analytic in the complex plane. In addition, $\underline{R}(z,\mu)$ is an analytic function of z [see eq(21b)].

4. FOURIER TRANSFORM INVERSION AND SINGULAR EIGENFUNCTION EXPANSION

It now becomes a relatively straightforward exercise to perform a Fourier inversion of eq(21a). For brevity, the full analysis is not presented here and the interested reader is referred to Ref. 12 for further details. The final solution can be written as

$$\vec{\Psi}(x,\mu) = \pm \sum_{j=1}^{J} e^{\mp x/\nu_j} \underline{\Phi}\left(\pm \nu_j, \mu\right) \underline{M}_{Lj\pm}^{-1} \vec{q} + \\ + \int_0^{\pm 1} d\nu e^{\mp x/\nu} \left[\underline{\Phi}(\nu,\mu) \underline{M}_L^{-1}(\nu) \right] \vec{q} \tag{24}$$

with + for $x > 0$ and − for $x < 0$ and

$$det \underline{\Lambda}_L(\nu_j) = 0, \quad j = 1,2,...J$$

$$\underline{M}_{Lj\pm}^{-1} \equiv \frac{2}{\nu_j^2} \underline{g}_L^{-1}(\nu_j, \nu_j \underline{\Sigma}) adj\left[\tilde{\underline{\Lambda}}_L^*(\nu_j) \right] \left[\frac{d\left| \tilde{\underline{\Lambda}}_L^* \right|}{d\nu} \right]_{\pm \nu_j}^{-1}$$

$$\underline{M}_L^{-1}(\nu) \equiv \frac{1}{\nu} \left[\underline{\Lambda}_L^{+-1}(\nu) \underline{\Theta}(\nu \underline{\Sigma}) \tilde{\underline{\Lambda}}_L^{*--1}(\nu) \right]$$

$$\underline{\Theta}(x\underline{D}) \equiv diag\left[\theta_1(d_1 x), ..., \theta_G(d_G x) \right]$$

where

$$\theta_g(x d_g) \equiv \begin{cases} 1, & x d_g \in \left[-1/\sigma_g, 1/\sigma_g \right] \\ 0, & x d_g \notin \left[-1/\sigma_g, 1/\sigma_g \right]. \end{cases}$$

All other symbols are defined in Ref. 12.

5. NUMERICAL IMPLEMENTATION AND DEMONSTRATION

While determining the solution directly in terms of singular eigenfunctions is theoretically satisfying, it is not so from a numerical viewpoint. To use the above analysis to gain some numerical leverage, a demonstration will now be performed. The scalar flux as represented by the first moment

$$\vec{\Psi}(x) \equiv \frac{1}{2\pi} \int_{-\infty}^{\infty} dk\, e^{-ikx} \underline{\Psi}_0(z) \vec{q} \tag{25}$$

where $\underline{\Psi}_0(z)$ is given by eq(14b) will be evaluated. The evaluation is performed via a numerical Fourier transform inversion as described in the author's various publications. The only new feature is an iteration on the

Gauss/Legendre quadrature order until each point is below a desired relative error.

The demonstration will be for a full scattering matrix with relatively high order anisotropy (up to L = 20). A fictitious set of cross sections is generated by

$$\Sigma_g = \frac{2(g+1)}{G}$$
$$C_{g,g',l} = c_S g_a^l \frac{2(g'+1)}{10G(g+g'+1)} \qquad (26)$$

where a Henyey-Greenstein scattering phase function with asymmetry factor g_a has been assumed.

Table 1 shows a comparison of the inversion for 5 desired errors ε. This table is presented in order to provide confidence in the inversion algorithm as implemented in the **FORTRAN** code **mg.f**. The problem considered was for 5 groups, g_a= 0.95, c_s = 0.95 and L = 10 for point source emission (see below). For all edit points, the fluxes are calculated to a higher accuracy than desired for all groups. This indicates the effectiveness of the quadrature order iteration.

Typically, as the scattering becomes more forward peaked, the scattering order L needs to be large and the inversion has increasing difficulty in converging. To attempt to improve the solution, a Wynn-epsilon algorithm was applied to the sequence of solutions specified by the order L of the scattering approximation. This algorithm makes use of the acceleration

$$\varepsilon_{-1}^{(L)} = 0,\ \varepsilon_0^{(L)} = S_L$$
$$\varepsilon_{k+1}^{(L)} = \varepsilon_k^{(L+1)} + \left[\varepsilon_k^{(L+1)} - \varepsilon_k^{(L)}\right]^{-1}$$

where S_L is the scalar flux at an edit point for the scattering order approximation L. The elements $\varepsilon_{k+1}^{(L)}$ are subsequent approximations of the approach of the flux to its limit as L approaches infinity. Table 2 shows a comparison with and without acceleration for scattering orders up to 20 near and far from the source. The accelerated values (shaded columns) are

improved over the original values especially near the source. However, they also begin degrade at high scattering order far from the source. Improvement by acceleration will be a subject of continued investigation.

The scalar flux from a plane source at $x = 0$ in group 3 is shown in Fig.1 for several degrees of decreasingly forward scattering (g_a = 0.95 to 0). The effect of anisotropy is surprisingly small.

Finally, the scalar flux from a point source is displayed in Figs. 2a,b. This flux is given by the plane/point transformation

$$\begin{aligned}\vec{\Psi}_{pt}(r) &\equiv -\frac{1}{2\pi r}\frac{d}{dr}\left[\frac{1}{2\pi}\int_{-\infty}^{\infty} dk\, e^{-ikr}\,\underline{\Psi}_0(z)\vec{q}\right] \\ &\equiv \frac{1}{2\pi r}\left[\frac{1}{2\pi}\int_{-\infty}^{\infty} dk\,\frac{e^{-ikr}}{z}\,\underline{\Psi}_0(z)\,\vec{q}\right].\end{aligned} \tag{27}$$

Again the effect is very small except near the source.

6. CONCLUSION

The solution to the multigroup neutron transport equations for isotropic source emission has been obtained as a singular eigenfunction expansion through a Fourier transform approach. This approach avoids the relatively obscure mathematics associated with singular eigenfunction and resolvant operators. For this reason, what has been presented has significant educational value. The resulting expression for the scalar flux was numerically evaluated using a numerical Fourier transform inversion. Selected results have been presented to demonstrate that benchmark quality is achieved and that relatively modest multigroup problems of 10 groups and moderately high order scattering (L = 10) can be treated. Computational times on an Ultra 5 Sun workstation for any of the benchmarks were modest with the last computation for the point source taking under 10 minutes.

REFERENCES

[1] R. Zelazny and A. Kuszell, *Ann Phys*., **16**, 81(1961).

[2] A. Leonard and J.H. Ferziger, *Nucl. Sci.& Eng*., **26**, 170(1966).

[3] C.E. Siewert and P.S. Seith , *Jour. Nucl. Ener*., **21**, 383(1967).

[4] T.Yoshimura and Katsuragi, *Nucl. Sci.& Eng*., **55**, 297(1968).

[5] J.K. Shultis, *Nucl. Sci.& Eng*., **38**, 83(1969).

[6] R.J. Reith Jr and C.E. Siewert, *Nucl. Sci.& Eng*., **47**, 156(1972).

[7] K.M. Case and P.F. Zweifel, *Linear Transport Theory*, Addison-Wesley, Pub. Co., Reading MA, (1967).

[8] R.L. Bowden, S. Sancaktar and P.F. Zweifel, *Jour. Math. Phys*.,17, 76(1976).

[9] R.L. Bowden, S. Sancaktar and P.F. Zweifel, *Jour. Math. Phys*.,17, 82(1976).

[10] B.D. Ganapol, TTSP,29,43-69 (2000).

[11] B.D. Ganapol and K. Parsons, M&C Topical Meeting, Madrid Spain, (1999).

[12] B.D. Ganapol, *Nucl. Sci.& Eng*., **137**, 200(2001).

Table 1

Desired Numerical Error

G= 5 g_a = 0.95 c_s = 0.95

ε = 1.0e-02

x\Gp	1	2	3	4	5
1.0000E-03	3.22**17**E+00	1.52**93**E-02	1.39**38**E-02	1.278**9**E-02	1.18**22**E-02
2.5008E+00	2.72**80**E-02	1.2494E-03	8.923**3**E-04	6.875**1**E-04	5.571**3**E-04
5.0005E+00	4.947**1**E-03	2.46**60**E-04	1.693**2**E-04	1.281**8**E-04	1.029**6**E-04
7.5003E+00	1.6085E-03	8.18**83**E-05	5.564**2**E-05	4.194**5**E-05	3.362**6**E-05
1.0000E+01	7.030**3**E-04	3.607**3**E-05	2.4416E-05	1.8377E-05	1.4721E-05

ε = 1.0e-03

1.0000E-03	3.219**2**E+00	1.526**9**E-02	1.391**7**E-02	1.2770E-02	1.1804E-02
2.5008E+00	2.7298E-02	1.2494E-03	8.9231E-04	6.8749E-04	5.5711E-04
5.0005E+00	4.9477E-03	2.4673E-04	1.6938E-04	1.2822E-04	1.0299E-04
7.5003E+00	1.6085E-03	8.1893E-05	5.5647E-05	4.1948E-05	3.3628E-05
1.0000E+01	7.030**3**E-04	3.6074E-05	2.4416E-05	1.8377E-05	1.4721E-05

ε = 1.0e-04

1.0000E-03	3.219**4**E+00	1.5272E-02	1.3918E-02	1.2770E-02	1.1804E-02
2.5008E+00	2.7298E-02	1.2494E-03	8.9231E-04	6.8749E-04	5.5711E-04
5.0005E+00	4.9477E-03	2.4673E-04	1.6938E-04	1.2822E-04	1.0299E-04
7.5003E+00	1.6085E-03	8.1893E-05	5.5647E-05	4.1948E-05	3.3628E-05
1.0000E+01	7.0304E-04	3.6074E-05	2.4416E-05	1.8377E-05	1.4721E-05

ε = 1.0e-05

1.0000E-03	3.2193E+00	1.5272E-02	1.3918E-02	1.2770E-02	1.1804E-02
2.5008E+00	2.7298E-02	1.2494E-03	8.9232E-04	6.8749E-04	5.5711E-04
5.0005E+00	4.9477E-03	2.4673E-04	1.6938E-04	1.2822E-04	1.0299E-04
7.5003E+00	1.6085E-03	8.1893E-05	5.5647E-05	4.1948E-05	3.3628E-05
1.0000E+01	7.0304E-04	3.6074E-05	2.4416E-05	1.8377E-05	1.4721E-05

ε = 1.0e-06

1.0000E-03	3.2193E+00	1.5272E-02	1.3918E-02	1.2770E-02	1.1804E-02
2.5008E+00	2.7298E-02	1.2494E-03	8.9232E-04	6.8749E-04	5.5711E-04
5.0005E+00	4.9477E-03	2.4673E-04	1.6938E-04	1.2822E-04	1.0299E-04
7.5003E+00	1.6085E-03	8.1893E-05	5.5647E-05	4.1948E-05	3.3628E-05
1.0000E+01	7.0304E-04	3.6074E-05	2.4416E-05	1.8377E-05	1.4721E-05

Table 2

Comparison of Accelerated and Unaccelerated

$G = 10$ $g_a = 0.75$ $c_s = 0.95$

$x = 0.01$

	gp 2		gp 10	
L\Gp	Original	Accelerated	Original	Accelerated
1	1.4135E-02	1.4135E-02	8.1778E-03	8.1778E-03
2	1.7242E-02	1.8118E-02	9.5230E-03	9.7878E-03
3	1.5620E-02	1.6176E-02	8.8616E-03	9.0796E-03
4	1.6533E-02	1.6204E-02	9.2139E-03	9.0916E-03
5	1.5993E-02	1.6196E-02	9.0163E-03	9.0883E-03
6	1.6322E-02	1.6322E-02	9.1308E-03	9.1308E-03
7	1.6116E-02	1.6196E-02	9.0628E-03	9.0882E-03
8	1.6248E-02	1.6197E-02	9.1039E-03	9.0884E-03
9	1.6163E-02	1.6196E-02	9.0787E-03	9.0883E-03
10	1.6218E-02	1.6196E-02	9.0943E-03	9.0883E-03
11	1.5225E-02	1.6196E-02	8.9078E-03	9.0883E-03
12	6.5794E-03	1.6197E-02	7.6393E-03	9.0884E-03
13	5.6287E-01	1.6196E-02	8.5951E-02	9.0883E-03
14	-2.0771E-01	1.6197E-02	-1.8916E-02	9.0885E-03
15	-8.9231E+01	1.6196E-02	-1.2155E+01	9.0882E-03
16	-7.8038E+04	1.6197E-02	-1.1275E+04	9.0885E-03
17	-1.6303E+04	1.6196E-02	-2.2076E+03	9.0883E-03
18	-4.1913E+03	1.6197E-02	-6.2490E+02	9.0884E-03
19	-2.0172E+01	1.6196E-02	3.2386E+01	9.0883E-03
20	-3.3334E+07	1.6197E-02	-5.0189E+06	9.0884E-03

$x = 10.0$

1	3.4441E-05	3.4441E-05	7.3952E-06	7.3952E-06
2	3.4338E-05	3.4339E-05	7.3885E-06	7.3885E-06
3	3.4339E-05	3.4339E-05	7.3885E-06	7.3885E-06
4	3.4339E-05	3.4339E-05	7.3885E-06	7.3885E-06
5	3.4339E-05	3.4339E-05	7.3885E-06	7.3885E-06
6	3.4339E-05	3.4339E-05	7.3885E-06	7.3885E-06
7	3.4339E-05	3.4339E-05	7.3885E-06	7.3885E-06
8	3.4339E-05	3.4339E-05	7.3885E-06	7.3885E-06
9	3.4339E-05	3.4339E-05	7.3885E-06	7.3885E-06
10	3.4339E-05	3.4339E-05	7.3885E-06	7.3885E-06
11	3.4339E-05	3.4339E-05	7.3885E-06	7.3885E-06
12	3.4339E-05	3.4339E-05	7.3885E-06	7.3885E-06
13	3.4339E-05	3.4339E-05	7.3885E-06	7.3885E-06
14	3.4339E-05	3.4339E-05	7.3885E-06	7.3885E-06
15	3.4339E-05	3.4339E-05	7.3885E-06	7.3885E-06
16	3.4339E-05	3.4339E-05	7.3885E-06	7.3885E-06
17	3.4339E-05	3.4339E-05	7.3885E-06	7.3885E-06
18	3.4339E-05	3.4339E-05	7.3885E-06	7.3885E-06
19	3.4339E-05	3.4339E-05	7.3885E-06	7.3885E-06
20	3.4340E-05	3.4339E-05	7.3887E-06	7.3885E-06

Fig. 1. Influence of anistropy for plane source

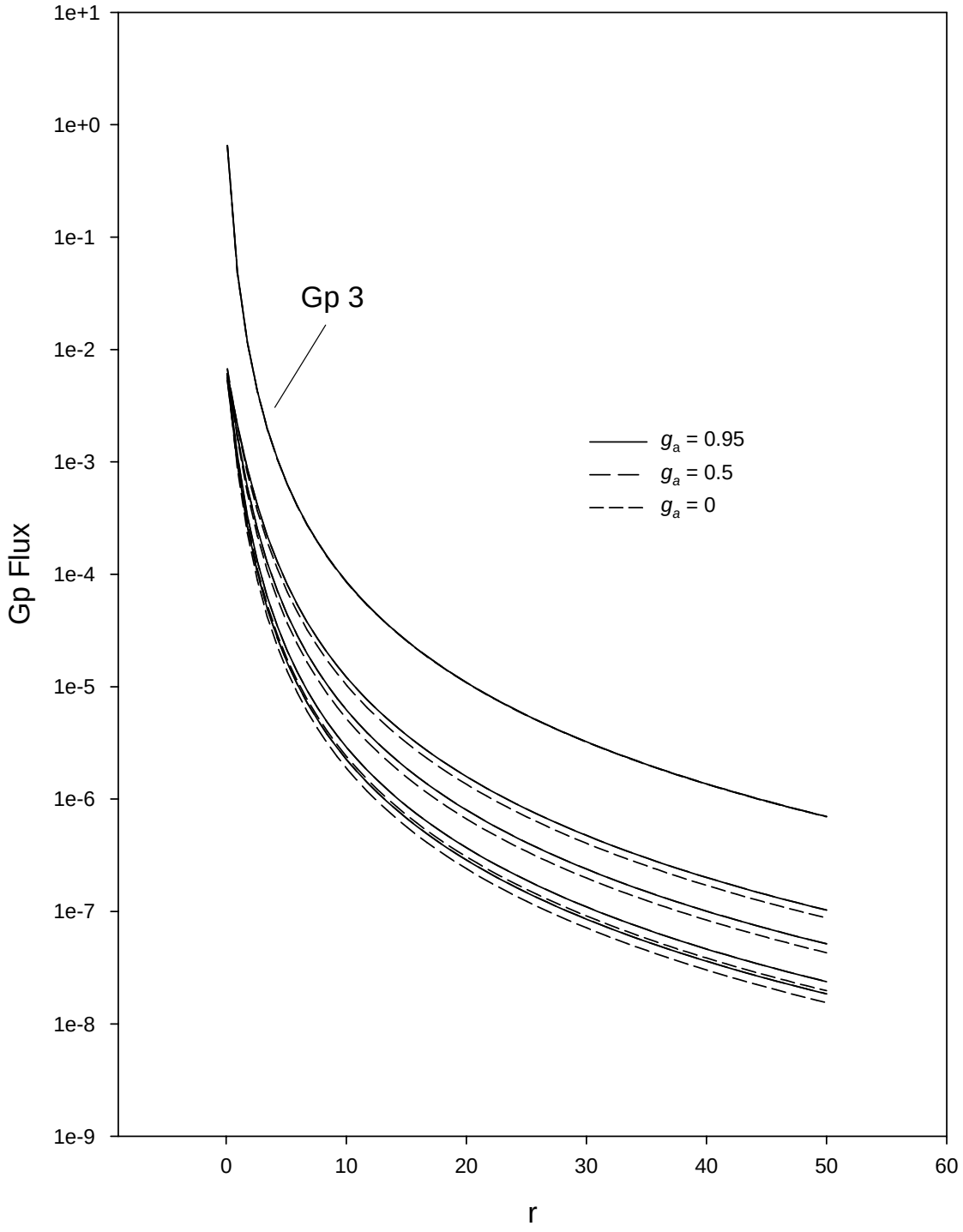

Fig. 2a. Influence of anistropy for a point source

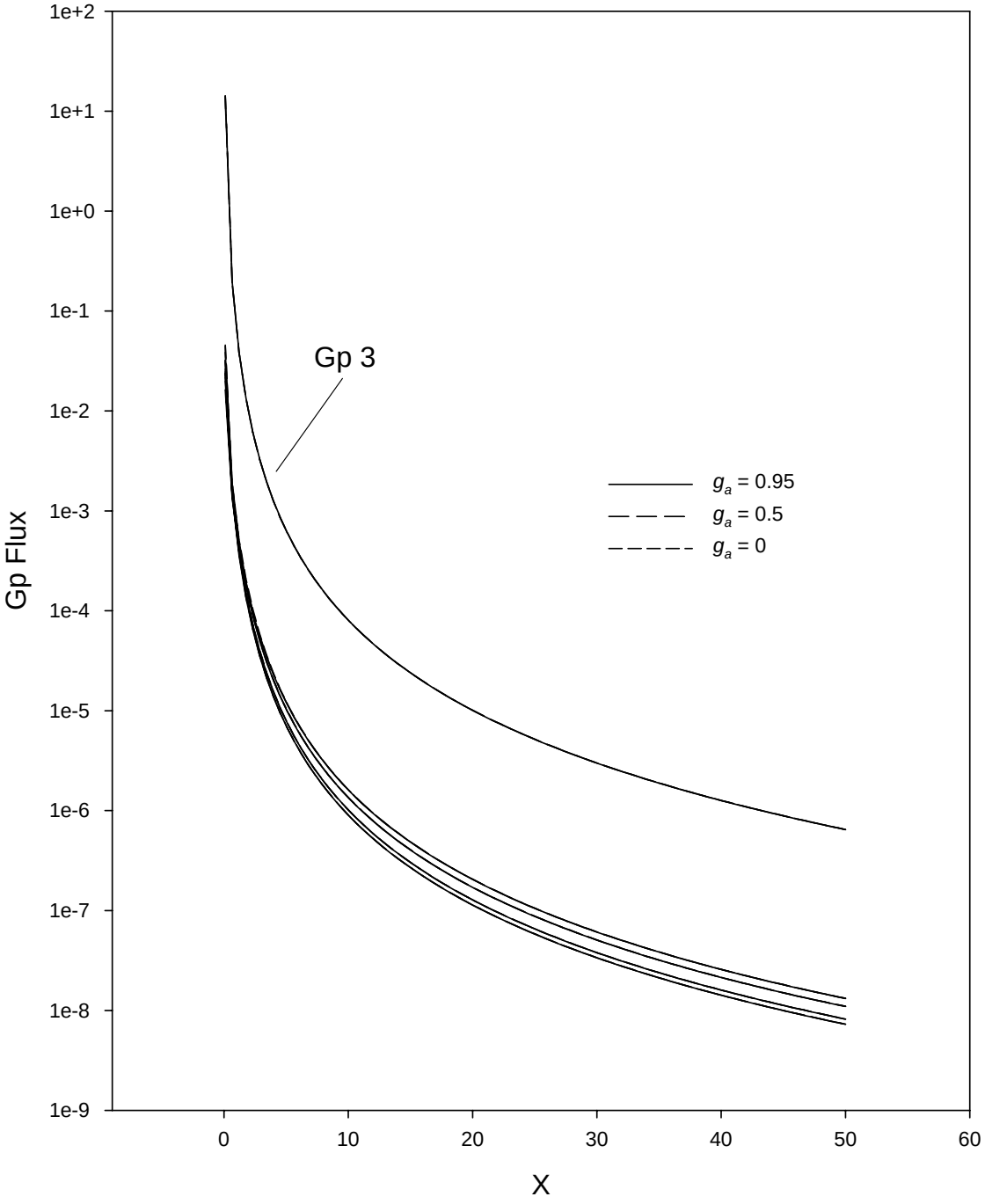

Fig 2b. Near point source

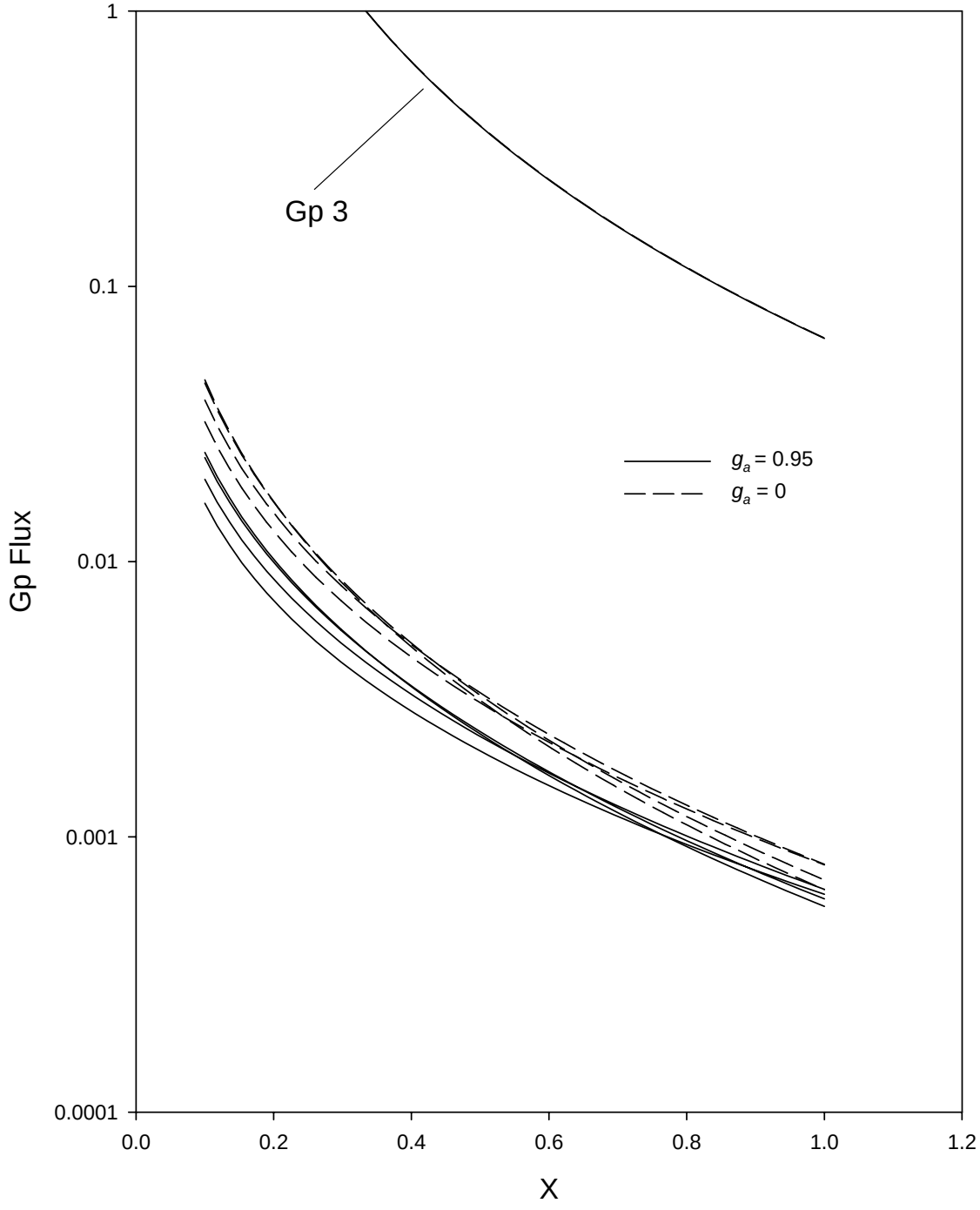

CHAPTER III

A HETEROGENEOUS MEDIUM ANALYTICAL BENCHMARK

1. INTRODUCTION

Assurance that particle transport methods are efficiently implemented and that current codes are adequately maintained is a major challenge facing today's power reactor and weapons communities. As used here, an analytical benchmark refers to highly accurate evaluations of analytical representations of solutions to the neutral particle transport equation. The primary advantage of an analytical benchmark is that its numerical evaluation occurs at the level of the solution rather than at the level of the integro-differential Boltzmann equation itself. Numerical evaluation generally occurs after the transport equation has been solved theoretically to obtain a solution representation continuous in the independent variables thus, in principle, avoiding discretization error altogether. Because of the requirement of an analytical solution however, only relatively limited transport scenarios can be treated. To some this may seem to be a major disadvantage of analytical benchmarks. To the code developer, simplicity by no means diminishes the usefulness of these benchmarks since transport codes *must* perform adequately for simple as well as comprehensive transport scenarios. Thus, comparisons to analytical benchmarks always provide diagnostic information about any comprehensive transport code by either uncovering errors or assessing performance. As will be demonstrated with this benchmark, the nature of transport problems that can be treated has become progressively more advanced since analytical benchmarks in neutron transport theory first appeared in 1953 [Case, 1953].

The benchmark considered, in this presentation, is for 1-D steady state monenergetic (one-group) neutral particle transport in an anisotropically scattering heterogeneous medium. A new Fourier transform inversion, to be employed in the Green's Function Method (GFM), generates the required analytical solution representation. This method effectively specifies the Green's function for a 1-D plane parallel medium, which when integrated over appropriate (unknown) boundary sources, gives the solution representation for the angular flux within a finite medium. The resulting integral equations are solved for the unknown boundary fluxes which then allows the determination of the interior fluxes via quadrature. A heterogeneous medium is accommodated through iteration of the boundary fluxes. A similar (but not the same) algorithm can be found in reference [Benoist, 1996]. The main difference between the algorithms is the use of a monomial expansion for the exiting fluxes rather than

the solution to an integral equation as proposed below. In addition, a more accurate numerical inversion is employed in this work and **BLUE** is available to the transport community.

2. THE GREEN'S FUNCTION METHOD: THEORY

2.1. Neutron transport equation in a slab: Placzek's Lemma

Only the transport of neutrons will be considered in the remainder of this presentation; however, the analysis remains valid for photon transport in the gray approximation and for electron transport for screened-Rutherford scattering with appropriate redefinition of the interaction parameters.

In general, we are interested in the solution to the following 1-D monoenergetic neutron transport equation:

$$\left[\mu\frac{\partial}{\partial x}+1\right]\Psi(x,\mu)=\frac{\omega}{2}\sum_{l=0}^{L}\omega_l P_l(\mu)\Psi_l(x) \qquad (1a)$$

where the flux moments are defined as

$$\Psi_l(x)\equiv\int_{-1}^{1}d\mu P_l(\mu)\Psi(x,\mu)\ . \qquad (1b)$$

The flux Ψ is to be determined for neutrons at the position x traveling in the direction μ resulting from sources at the slab boundaries for a slab of thickness a. General anisotropic scattering is assumed through a truncated (at L) Legendre polynomial (P_l) series expansion (with coefficient ω_l) of the differential scattering cross section. The number of secondaries per collision is ω and all distances are measured in terms of the total mean free path. Equation (1a) is to be solved with known fluxes illuminating the slab surfaces

$$\Psi(0,\mu)=F_L(\mu),\ \ \mu>0,\Psi(a,\mu)=F_R(-\mu),\ \ \mu<0. \qquad (1c)$$

From the well-known lemma of G. Placzek [Case, 1953], the boundary conditions can be replaced by an equivalent volume source of the form

$$S(x,\mu)\equiv\mu\Psi(0,\mu)\delta(x)-\mu\Psi(a,\mu)\delta(x-a) \qquad (2b)$$

to give the following transport equation: to be solved:

$$\left[\mu\frac{\partial}{\partial x}+1\right]\Psi(x,\mu)=\frac{\omega}{2}\sum_{l=0}^{L}\omega_l P_l(\mu)\Psi_l(x)+S(x,\mu)\ .$$

2.2. Solution representation via Green's functions

A solution representation is obtained by first expressing the Green's function in plane-parallel geometry as the solution to the following transport equation:

$$\left[\mu\frac{\partial}{\partial x}+1\right]G(x,\mu;\mu_0)=\frac{\omega}{2}\sum_{l=0}^{L}\omega_l P_l(\mu)G_l(x;\mu_0)+\delta(\mu-\mu_0)\delta(x) \qquad (3)$$

with moments $G_l(x;\mu_0)$ and finiteness condition $\lim_{|x|\to\infty} G(x,\mu;\mu_0)<\infty$. Then multiplying eqs(3) by the source $S(x-x',\mu')$ and integrating over all x' and μ' gives a representation of the solution in terms of the Green's function

$$\Psi(x,\mu)=\int_{-1}^{1}d\mu'\int_{-\infty}^{\infty}dx' S(x-x',\mu')G(x',\mu;\mu') \ . \qquad (4)$$

By substitution of *S* from eq(2b) along with the decomposition of the Green's function into collided (G_c) and uncollided components, performing the integrations over the delta functions and replacing *x* by 0^+ and a^-, eq(4) becomes

$$\begin{aligned}\Psi(0^+,-\mu)=&\ e^{-a/\mu}F_R(\mu)+\int_0^1 d\mu'\mu' F_L(\mu')G_c(0^+,-\mu;\mu')+\int_0^1 d\mu'\mu' F_R(\mu')G_c(a,\mu;\mu')-\\&-\int_0^1 d\mu'\mu' G_c(0^+,-\mu;-\mu')\Psi(0^+,-\mu')-\int_0^1 d\mu'\mu' G_c(a,\mu;-\mu')\Psi(a^-,\mu')\end{aligned} \qquad (5a)$$

$$\begin{aligned}\Psi(a^-,\mu)=&\ e^{-a/\mu}F_L(\mu)+\int_0^1 d\mu'\mu' F_L(\mu')G_c(a,\mu;\mu')+\int_0^1 d\mu'\mu' F_R(\mu')G_c(0^+,-\mu;\mu')-\\&-\int_0^1 d\mu'\mu' G_c(a,\mu;-\mu')\Psi(0^+,-\mu')-\int_0^1 d\mu'\mu' G_c(0^+,-\mu;-\mu')\Psi(a^-,\mu')\ .\end{aligned} \qquad (5b)$$

The corresponding scalar flux is obtained by integration over μ.

Once the Green's function has been determined, eqs(5) are solved as coupled integral equations for the exiting fluxes. Thus, to this point, the two numerical methods associated with the Green's function method are the determination of the Green's function and the solution to two coupled integral equations.

For future convenience in treating heterogeneous slab geometry, the incoming flux at *x*=0 will be assumed to contain a monodirectional component which is separated from the diffuse component

$$F_L(\mu)=\alpha_L\delta(\mu-\mu_0)+\tilde{F}_L(\mu) \ .$$

When substituted into eqs(5), we obtain the following modified integral equations for the boundary fluxes:

$$\begin{aligned}\Psi_c(0^+,-\mu)=&\ e^{-a/\mu}F_R(\mu)+\alpha_L\mu_0\left[G_c(0^+,-\mu;\mu_0)-e^{-a/\mu_0}G_c(a,\mu;-\mu_0)\right]+\\&+\int_0^1 d\mu'\mu'\tilde{F}_L(\mu')G_c(0^+,-\mu;\mu')+\int_0^1 d\mu'\mu' F_R(\mu')G_c(a,\mu;\mu')-\\&-\int_0^1 d\mu'\mu' G_c(0^+,-\mu;-\mu')\Psi_c(0^+,-\mu')-\int_0^1 d\mu'\mu' G_c(a,\mu;-\mu')\Psi_c(a^-,\mu')\end{aligned} \qquad (6a)$$

$$\begin{aligned}\Psi_c(a^-,\mu)=&\ e^{-a/\mu}\tilde{F}_L(\mu)+\alpha_L\mu_0\left[G_c(a,\mu;\mu_0)-e^{-a/\mu_0}G_c(0^+,-\mu;-\mu_0)\right]+\\&+\int_0^1 d\mu'\mu'\tilde{F}_L(\mu')G_c(a,\mu;\mu')+\int_0^1 d\mu'\mu' F_R(\mu')G_c(0^+,-\mu;\mu')-\\&-\int_0^1 d\mu'\mu' G_c(a,\mu;-\mu')\Psi_c(0^+,-\mu')-\int_0^1 d\mu'\mu' G_c(0^+,-\mu;-\mu')\Psi_c(a^-,\mu')\end{aligned} \qquad (6b)$$

where $\Psi_c(x,\mu)$ is the collided component in the decomposition

$$\Psi(x,\mu) = \alpha_L e^{-x/\mu_0}\delta(\mu-\mu_0) + \Psi_c(x,\mu) \ .$$

2.3. Determination of the Green's function: Theory

When eq(3) is operated on by a Fourier transform, there results

$$(1+ik\mu)G(k,\mu;\mu_0) = \frac{\omega}{2}\sum_{l=0}^{L}\omega_l P_l(\mu)G_l(k;\mu_0) + \delta(\mu-\mu_0) \ , \qquad (7a)$$

where the transformed moments are

$$G_l(k;\mu_0) \equiv \int_{-\infty}^{\infty} dx\, e^{-ikx} G_l(x;\mu_0) \qquad (7b)$$

and the Fourier transform of the flux is defined by

$$G(k,\mu;\mu_0) \equiv \int_{-\infty}^{\infty} dx\, e^{-ikx} G(x,\mu;\mu_0) \ . \qquad (7c)$$

Note, that in this presentation, the transformed Green's function is implied when the argument is either *k* or *z*. Once the image functions are known explicitly, the angular and scalar Green's functions are determined from their respective inversions as

$$G(x,\mu;\mu_0) \equiv \frac{1}{2\pi}\int_{-\infty}^{\infty} dk\, e^{ikx} G(k,\mu;\mu_0) \ , \quad G(x;\mu_0) \equiv \frac{1}{2\pi}\int_{-\infty}^{\infty} dk\, e^{ikx} G(k;\mu_0).$$

Since the image functions are much too complicated for the inversions to be performed analytically in terms of special functions, a numerical inversion will be employed.

When eq(7a) is divided by $(1+ik\mu)$ and projected over the Legendre polynomials, the following closed system of equations is obtained for the transformed moments:

$$G_j(k;\mu_0) = \omega\sum_{l=0}^{L}\omega_l L_{jl}(k)G_l(k;\mu_0) + \frac{P_j(\mu_0)}{1+ik\mu_0} \qquad (8a)$$

for $0 \le j \le L$ with the matrix elements defined as

$$L_{jl}(k) = \frac{1}{2}\int_{-1}^{1} d\mu \frac{P_j(\mu)P_l(\mu)}{1+ik\mu} \ . \qquad (8b)$$

In principle, eq(8a) can be solved for the transformed moments through matrix inversion. While this approach has proven to generally result in an accurate numerical algorithm for low order scattering ($L < 5$), theoretically it is less than satisfying since the transform of the moments is not expressed explicitly. For this reason, an alternative formulation will be followed to obtain an explicit moment representation through the solution of a recursion relation.

A recurrence relation satisfied by the moments can be obtained by projection of eq(7a) over the Legendre polynomials

$$zh_l G_l(k;\mu_0) + (l+1)G_{l+1}(k;\mu_0) + lG_{l-1}(k;\mu_0) = z(2l+1)P_l(\mu_0) \qquad (9)$$

where

$$z \equiv 1/ik \text{ and } h_l \equiv 2l+1-\omega\omega_l \quad .$$

From a rather involved derivation making use of Chandrasekhar polynomials of the first (g_l) and second (ρ_l) kinds [Inonu, 1970] and an auxiliary transport solution for isotropic source emission, the following new representation of the transform of the l-th moment is obtained [Ganapol, 1998]:

$$G_l^L(k;\mu_0) \equiv G_l^L(-z;\mu_0) = \frac{z}{z+\mu_0}\left\{\begin{array}{l} P_l(\mu_0) + \omega g_l(-z) f_L(-z;\mu_0) - \\ \quad -\omega\left[\rho_l(-z) g_l(-z,\mu_0) - g_l(-z) h_l(-z,\mu_0)\right] \end{array}\right\} \qquad (10)$$

where

$$f_L(-z;\mu_0) \equiv g_L(-z,\mu_0) G_0(-z) - h_L(-z,\mu_0), \; G_0(z) \equiv \frac{\hat{g}_L(z)}{\Lambda_L(z)}$$

$$\hat{g}_L(z) \equiv (L+1)\left[\rho_{L+1}(z)Q_L(z) - \rho_L(z)Q_{L+1}(z)\right], \; \Lambda_L(z) \equiv (L+1)\left[g_{L+1}(z)Q_L(z) - g_L(z)Q_{L+1}(z)\right]$$

$$g_L(z,\mu) \equiv \sum_{l=0}^{L} \omega_l P_l(\mu) g_l(z), \quad h_L(z,\mu) \equiv \sum_{l=0}^{L} \omega_l P_l(\mu)\rho_l(z).$$

Q_L is the Legendre function of the second kind of order L and the Chandrasekhar polynomials of the first and second kinds satisfy the following recursion relations:

$$-zh_l g_l(z) + (l+1)g_{l+1}(z) + lg_{l-1}(z) = 0, \; g_0(z) \equiv 1 \qquad (11a)$$

$$-zh_l \rho_l(z) + (l+1)\rho_{l+1}(z) + l\rho_{l-1}(z) = 0, \; \rho_0(z) \equiv 0, \; \rho_1(z) \equiv 1 \; . \qquad (11b)$$

A superscript L on the moment G_l indicating scattering order has been included for clarity of the analysis to follow.

While eq(10) is explicit, it is mainly of theoretical interest and is not particularly useful for numerical purposes. The numerical difficulty lies in the polynomial nature of the subtracted terms which leads to catastrophic round off error. Thus, an alternative representation has been sought. After some lengthy algebra, we find

$$G^L(k,\mu;\mu_0) = G^0(k;\mu,\mu_0) + \frac{\omega}{2}\left[\frac{z}{z+\mu}\right]\left[\frac{z}{z+\mu_0}\right]\sum_{l=1}^{L}\omega_l\left[\frac{\xi_l(-z,\mu)}{\Lambda_l(-z)}\right]\left[\frac{\xi_l(-z,\mu_0)}{\Lambda_{l-1}(-z)}\right] \qquad (12a)$$

where $G^0(k;\mu,\mu_0)$ is the transformed solution for isotropic scattering

$$G^0(k,\mu;\mu_0)=\left[\frac{z}{z+\mu_0}\right]\delta(\mu-\mu_0)+\frac{\omega}{2}\left[\frac{z}{z+\mu}\right]\left[\frac{z}{z+\mu_0}\right]+ \\ +\frac{\omega}{2}\left[\frac{z}{z+\mu}\right]\left[\frac{z}{z+\mu_0}\right]\left[\frac{-\omega z Q_0(-z)}{1+\omega z Q_0(-z)}\right]\ldots \tag{12b}$$

The transformed scalar flux is found simply by integration

$$G^L(k,\mu_0)=G^0(k;\mu_0)-\omega\left[\frac{z^2}{z+\mu_0}\right]\sum_{l=1}^{L}\omega_l\left[\frac{Q_l(-z)}{\Lambda_l(-z)}\right]\left[\frac{\xi_l(-z,\mu_0)}{\Lambda_{l-1}(-z)}\right] \tag{13a}$$

with

$$G^0(k;\mu_0)=\left[\frac{z}{z+\mu_0}\right]+\left[\frac{z}{z+\mu_0}\right]\left[\frac{\omega z Q_0(-z)}{1+\omega z Q_0(-z)}\right]\ . \tag{13b}$$

To the author's knowledge, these image functions in the above forms have never before been published.

3. THE GREEN'S FUNCTION METHOD: NUMERICAL IMPLEMENTATION

3.1. Numerical Fourier Transform Inversion

The evaluation of the following improper integral constitutes the numerical Fourier inversion:

$$f(x)\equiv\frac{1}{2\pi}\int_{-\infty}^{\infty}dk\,e^{ikx}\bar{f}(k)\ ; \tag{14}$$

k is a real variable. For clarity, the image function has been defined with an overbar. Integrals of this type are well known to be difficult to numerically evaluate because of the infinite integration range compounded by the unending oscillations of the integrand. Needless to say, special care must be exercised.

By noting that $\mathrm{Re}[f(k)]$ and $\mathrm{Im}[f(k)]$ are even and odd functions of *k* respectively, the inversion integral can be rewritten as

$$f(x)\equiv\frac{1}{\pi}\int_0^{\infty}dk\,\{\mathrm{Re}[\bar{f}(k)]\cos(kx)-\mathrm{Im}[\bar{f}(k)]\sin(kx)\}\ . \tag{15}$$

From a change of variable and reformulation of the improper integral as an infinite series, there results for $x\neq 0$

$$f(x)\equiv\frac{1}{\pi x}\sum_{j=0}^{\infty}(-1)^j\int_0^{\pi}du\,\{\mathrm{Re}[\bar{f}((u+j\pi)/x)]\cos(u)-\mathrm{Im}[\bar{f}((u+j\pi)/x)]\sin(u)\}\ . \tag{16}$$

The integrals in each term are to be evaluated by a shifted Gauss/Legendre (GL) quadrature of order m_b. The convergence of the infinite series is accelerated through the Wynn-epsilon algorithm [Graves, 1972] which is the primary reason that this numerical procedure can be used at all.

For the special case $x = 0$, a change of variables gives

$$f(0) = \frac{2}{\pi}\int_{-1}^{1} dt \frac{1}{(1-t)^2} \mathrm{Re}\left[\bar{f}\left(\frac{1+t}{1-t}\right)\right] . \qquad (17)$$

This integral is evaluated as a GL-quadrature on the interval [-1,1]. In this way, the apparent singularity is effectively ignored. This expression is numerically advantageous since it does not involve an infinite series evaluation. For this reason, an algorithm has been crafted around eq(17) to evaluate the angular Green's function for $x \neq 0$ as will be discussed.

3.2. Fourier inversion

The Green's function determination (collided contribution only) is partitioned into 4 components depending on the sign of the independent variables *x* and μ. These components correspond to the 4 quadrants ++,+-,-+,-- for *x* an μ respectively. In particular, to determine the exiting angular fluxes [eqs(6)], only the Green's functions in quadrants 1 and 4 are required. This approach provides a distinct numerical advantage in which the numerically convenient Green's function evaluation at $x = 0$ can be utilized as will now be demonstrated.

The infinite medium Green's function solution can be reformulated as two half-space problems connected at the interface ($x = 0$) by a source condition. Assuming that the Green's function at $x = 0$ is known results in the following integral equation between the Green's functions of quadrants 1 and 4:

$$\begin{aligned} G_c(-x,-\mu;\mu_0) &= e^{-x/\mu}\Theta(x/\mu)G_c(0^-,-\mu;\mu_0) + \\ &+ \int_0^1 d\mu'\mu' G_c(0^-,-\mu';\mu_0)G_c(x,\mu;\mu') - \int_0^1 d\mu'\mu' G_c(0^-,\mu';\mu_0)G_c(-x,-\mu;\mu'). \end{aligned} \qquad (18)$$

For completeness, the representation of the Green's function at $x = 0$ is repeated here

$$G_c(0^-,\mu;\mu_0) = \frac{2}{\pi}\int_{-1}^{1} dt \frac{1}{(1-t)^2} \mathrm{Re}\left[\bar{G}_c\left(\frac{1+t}{1-t},\mu;\mu_0\right)\right] .$$

Thus, with the knowledge of $G_c(0^-,\mu;\mu_0)$ and $G_c(x,\mu;\mu')$ (in the first quadrant), eq(18) can be solved for $G_c(-x,-\mu;\mu')$ (in the fourth quadrant). By approximating the integrals in terms of a shifted GL-quadrature of order L_m, eq(18) can be recast as the matrix equation

$$\begin{aligned} &\sum_{l=1}^{L_m}\left[\delta_{j,l} + \omega_l\mu_l G_c(0^-,\mu_l;\mu_j)\right]G_4(\mu_j) = \\ &\qquad = e^{-x/\mu}G_c(0^-,-\mu;\mu_j) + \sum_{l=1}^{L_m}\omega_l\mu_l G_1(\mu_l)G_c(0^-,-\mu_l;\mu_j) \end{aligned} \qquad (19)$$

where

$$G_1(\mu_j) \equiv G_c(x, \mu; \mu_j)\,,\; G_4(\mu_j) \equiv G_c(-x, -\mu; \mu_j)\,.$$

Note that x and μ are just parameters in this formulation.

Similarly, the scalar flux is obtained from integration of eq(18) over μ

$$\begin{aligned} G_c(-x; \mu_0) &= \int_0^1 d\mu e^{-x/\mu} G_c(0^-; \mu_0) + \\ &+ \int_0^1 d\mu' \mu' G_c(0^-, -\mu'; \mu_0) G_c(x; \mu') - \int_0^1 d\mu' \mu' G_c(0^-, \mu'; \mu_0) G_c(-x; \mu'). \end{aligned} \tag{20}$$

Therefore, from a knowledge of $G_c(0^-, \mu; \mu_0)$ and $G_c(x; \mu')$, $G_c(-x; \mu')$ is obtained as the solution of

$$\begin{aligned} &\sum_{l=1}^{L_m} \left[\delta_{j,l} + \omega_l \mu_l G_c(0^-, \mu_l; \mu_j)\right] G_2(\mu_l) = \\ &\quad = \sum_{l=1}^{L_m} \omega_l e^{-x/\mu_l} G_c(0^-; \mu_j) + \sum_{l=1}^{L_m} \omega_l \mu_l G_c(0^-, \mu_l; \mu_j) G_1(\mu_l) \end{aligned} \tag{21}$$

with

$$G_1(\mu_j) \equiv G_c(x; \mu_j)\,, G_2(\mu_j) \equiv G_c(-x; \mu_j)\,.$$

3.3. Solution for the exiting angular and scalar fluxes

A. Exiting angular fluxes

Rather than solve the coupled integral equations [eqs(6)] directly for the exiting angular fluxes, they can be manipulated into two uncoupled integral equations. If $r_\pm(\mu)$ is defined as

$$r_\pm(\mu) \equiv \Psi_c(0^+, -\mu) \pm \Psi_c(a^-, \mu)\,, \tag{22}$$

eqs(6a) and (6b) can be added and subtracted to give

$$\begin{aligned} r_\pm(\mu) &= e^{-a/\mu}\left[\tilde{F}_L(\mu) \pm F_R(\mu)\right] + \int_0^1 d\mu' \mu' \left[\tilde{F}_L(\mu') \pm F_R(\mu')\right]\left[G_c(0^+, -\mu; \mu') \pm G_c(a, \mu; \mu')\right] + \\ &+ \alpha_L \mu_0 \left\{\left[G_c(0^+, -\mu; \mu_0) \pm G_c(a, \mu; \mu_0)\right] - e^{-a/\mu_0}\left[G_c(a, -\mu; \mu_0) \pm G_c(0^+, \mu; -\mu_0)\right]\right\} - \\ &- \int_0^1 d\mu' \mu' \left[G_c(0^+, -\mu; -\mu') \pm G_c(a, \mu; -\mu')\right] r_\pm(\mu'') \end{aligned} \tag{23}$$

When the integrals are approximated by a GL-quadrature and μ is evaluated at the abscissa, the following matrix equations result:

$$\sum_{l=1}^{L_m}\left\{\delta_{l,j}+\omega_l\mu_l\left[G_c\left(0^+,-\mu_j;-\mu_l\right)\pm G_c\left(a,\mu_j;-\mu_l\right)\right]\right\}_l r_{\pm j}= \tag{24a}$$

$$=e^{-a/\mu_j}\left[\tilde{F}_L\left(\mu_j\right)\pm F_R\left(\mu_j\right)\right]+\sum_{l=1}^{L_m}\omega_l\mu_l\left[\tilde{F}_L\left(\mu_l\right)\pm F_R\left(\mu_l\right)\right]\left[G_c\left(0^+,-\mu_j;\mu_l\right)\pm G_c\left(a,\mu_j;\mu_l\right)\right]+$$

$$+\alpha_L\mu_0\left\{\left[G_c\left(0^+,-\mu_j;\mu_0\right)\pm G_c\left(a,\mu_j;\mu_0\right)\right]-e^{-a/\mu_0}\left[G_c\left(a,-\mu_j;\mu_0\right)\pm G_c\left(0^+,\mu_j;-\mu_0\right)\right]\right\}.$$

Finally, the fluxes are recovered from

$$\Psi_c\left(0^+,-\mu_j\right)=\frac{\left[r_{+j}+r_{-j}\right]}{2},\ \Psi_c\left(a^-,-\mu_j\right)=\frac{\left[r_{+j}-r_{-j}\right]}{2} \tag{24b}$$

B. Interior scalar flux

The interior scalar flux is obtained from eq(6a) as

$$\Psi(x)=\alpha_L\mu_0\left[G(x;\mu_0)-e^{-a/\mu_0}G(a-x;-\mu_0)\right]+$$

$$+\int_0^1 d\mu'\mu'\left[\tilde{F}_L(\mu')G(x;\mu')+F_R(\mu')G(a-x;\mu')\right]- \tag{25}$$

$$-\int_0^1 d\mu'\mu'\left[G(x;-\mu')\Psi_c\left(0^+,-\mu'\right)+G(a-x;-\mu')\Psi_c(a,\mu')\right].$$

A reduction in numerical effort is achieved for uniform spatial edit intervals by evaluating $\Psi(x)$ and $\Psi(a-x)$ simultaneously. Since

$$\Psi(a-x)=\alpha_L\mu_0\left[G(a-x;\mu_0)-e^{-a/\mu_0}G(x;-\mu_0)\right]+$$

$$+\int_0^1 d\mu'\mu'\left[\tilde{F}_L(\mu')G(a-x;\mu')+F_R(\mu')G(x;\mu')\right]- \tag{26}$$

$$-\int_0^1 d\mu'\mu'\left[G(a-x;-\mu')\Psi_c\left(0^+,-\mu'\right)+G(x;-\mu')\Psi_c(a,\mu')\right]$$

and if

$$q_\pm(x)\equiv\Psi(x)\pm\Psi(a-x)\ ,$$

then adding and subtracting eqs(25) and (26) gives

$$q_\pm(x)=\alpha_L\mu_0\left\{\left[G(x;\mu_0)\pm G(a-x;\mu_0)\right]-e^{-a/\mu_0}\left[G(a-x;-\mu_0)\pm G(x;-\mu_0)\right]\right\}+$$

$$+\int_0^1 d\mu'\mu'\left\{\left[\tilde{F}_L(\mu')\pm F_R(\mu')\right]\left[G(x;\mu')\pm G(a-x;\mu')\right]\right\}- \tag{27a}$$

$$-\int_0^1 d\mu'\mu'\left[G(x;-\mu')\pm G(a-x;-\mu')r_\pm(\mu')\right].$$

Therefore

$$\Psi(x)=\frac{\left[q_+(x)+q_-(x)\right]}{2},\qquad \Psi(a-x)=\frac{\left[q_+(x)-q_-(x)\right]}{2}\ ,$$

and the evaluation of $\Psi(x)$ is required at only half the number of edit points for uniform spatial edit intervals.

C. Auxiliary functions

Several auxiliary functions are required in order to evaluate the integrands for the Fourier inversions for the angular and scalar fluxes. In the evaluation of eqs(12) and (13), both the Legendre function of the second kind and the Chandrasekhar g-polynomial are necessary. The Legendre function of the second kind for a complex variable z is evaluated via the usual recurrence relation. The recurrence is run in the forward direction for $|z| < 1$ and in the backward direction for $|z| > 1$. The g-polynomial is obtained from eq(11a) in the forward direction. Note that the ρ-polynomial is not required and is mainly of theoretical interest.

4. COMPUTATIONAL STRATEGIES

4.1. Evaluation of Fourier transforms

In order to make the **BLUE** analytical benchmark as efficient as possible, special treatment of the evaluation of eqs(12) and (13) is required for the Fourier inversion. In particular, for a given quadrature order and position x, all complex quantities independent of μ and μ_0 need be calculated only once for each desired edit and stored. Thus, the necessary Q_l and g_l are determined once per x saving a significant amount of computational effort given the heavy reliance on iteration required for benchmark quality results.

4.2. Global $L2$ and L_{inf} relative errors

One possible measure of error used to specify the accuracy of a benchmark is the global $L2$ error. Global, here, refers to a macroscopic error over either the angular or spatial edit grids. The $L2$-error is defined as over an edit grid and between iterations

$$e_2 \equiv \left\{ \frac{1}{M} \sum_{i=1}^{M} \left[\frac{\left[f^k(y_i) - f^{k-1}(y_i) \right]}{f^k(y_i)} \right]^2 \right\}^{1/2} . \qquad (28)$$

where k indicates the k^{th} iterate and the summation is over either the angular or spatial edit grids. This expression holds for both inner slab and outer quadrature iterations, which are to be discussed in the following sections.

In addition to the $L2$ error, L_{inf}-error, called the maximum relative error for the angular or scalar fluxes between iterations, is defined as the maximum relative error occurring over the angular or spatial edit grids respectively. The maximum relative error is more conservative then the $L2$ relative error.

4.3. Outer quadrature iteration

As is evident, an analytical benchmark requires numerical evaluation as does any solution to the transport equation. Both the determination of the Green's functions and the exiting fluxes requires numerical quadrature. The difference, however, between an analytical benchmark and a corresponding numerical transport solution, say as given by an SN algorithm, is that errors associated with an analytical benchmark are more easily controlled automatically than those resulting from spatial and angular discretizations.

To ensure benchmark quality results, a compound iterative strategy is followed. The desired benchmark solution is recalculated by increasing the quadrature order used to determine the Green's functions and the exiting fluxes until convergence. This is the first of two iteration schemes and is called the outer quadrature iteration. In this iteration, the quadrature order L_m [i.e., in eqs(19),(21) and (24a)] is advanced until the exiting angular fluxes on the angular edit grid have converged to the desired relative error. Upon angular flux convergence, the interior scalar flux is then determined with increasing quadrature order until convergence on the spatial edit grid. "Engineering convergence", defined as the agreement between two consecutive approximations to within a specified global $L2$ or L_{inf} relative error as defined above, terminates the computation.

4.4. Inner slab iteration

The theory and numerical implementation discussed in sections **I** and **II** have been concerned with a single homogeneous medium. An iterative strategy has been devised to treat a heterogeneous medium consisting of contiguous homogeneous slabs. The slabs are connected through the boundary conditions $\tilde{F}_L, F_R$. For a particular slab, the incoming flux at $x = 0$ is the transmitted flux from the adjacent slab say to the left, and at $x = a$ the reflected flux from the adjacent slab to the right. Similarly, the exiting fluxes from the slab of interest are the sources for adjacent slabs. Since only the boundary conditions at the slabs bordering on a vacuum are known, an iterative procedure, called the slab inner iteration, has been specified to determine the unknown interior surface sources. The slab inner iteration is performed within each quadrature iteration. At each step of the inner iteration, the boundary conditions are updated. In general, the inner iteration need not be taken to convergence since the quadrature order has not yet fully converged. For a full benchmark calculation, a maximum of 15 inner slab iterations is allowed.

5. Benchmark Demonstrations

5.1. Multiple slabs demonstration

A multiple slab benchmark was run for slabs with the following material properties:

Slab	a	ω	g	L
1	1.0	0.95	0.8	10
2	0.1	0.15	0.1	3
3	4.0	0.90	0.6	8
4	2.0	0.30	0.7	7

A Henyey-Greenstein (H-G) scattering kernel of order L has been assumed ($\omega_l=g^l$). Table 1 shows the scalar flux within the four slabs for two cases for a normally incident source on the left boundary of slab 1. The first case is for a desired relative error of 10^{-5} while the second case is for a relatively large quadrature order (45) and is expected to be correct to all digits shown. In general, the accuracy of the first case is as expected in comparison with the second. A slight discrepancy in the last place at the first and last slab boundaries (almost within the desired relative error) can be observed in the first case however. This discrepancy is eliminated with higher quadrature order.

5.2. Benchmark Comparisons with ONEDANT and MCNP

A deep penetration problem for a 150mfp thick homogeneous slab was chosen for comparison purposes. This problem stresses any numerical method since the neutrons experience 23 orders of attenuation from surface to surface. The slab is assumed to be primarily scattering with $\omega = 0.9$ and to have a mildly forward peaked H-G kernel with $g = 0.6$ and $L = 10$. A unit source is normally incident on the left surface. For the analytical benchmark calculation, the medium was divided into 5 regions for efficiency of convergence. Apparently, the benchmark could not handle 23 orders of attenuation directly. Since an iterative procedure for the surface sources is used, partitioning the slab requires convergence for smaller interior slabs which is less demanding than for the entire slab. **ONEDANT** calculations were performed for several numerical configurations. In particular, the medium was divided into 15000 mesh cells each of thickness Δx=0.01mfp and standard quadrature sets of double Gauss (DG) for N=96 and N=200 were used. Cases using Lobotto sets were also run. In addition, several new features were introduced to make the comparisons more meaningful. Specifically, the angular edit grid was added to the quadrature set with (near) zero weights in order to avoid the need to interpolate between

quadrature angles. Also an attempt was made to standardize the source direction to be perpendicular ($\mu = 1$) to the free surface. Thus, $\mu = 1$ was input with (near) zero weight and the source was, for some cases, specified to be at this quadrature point. Finally, both the diamond difference (DD) and linear discontinuous (LD) spatial differencing schemes were tested.

Tables 2a,b,c show angular exiting and scalar flux comparisons where the ANB column is the analytical benchmark. All digits shown are believed to be correct. The column labeled SLD200^{+} is the result for Lobatto quadrature with LD and with edit angles added at zero weight. Except for the grazing angle ($\mu = 0$), the agreement with ANB is excellent. Even better agreement is observed for column SLD200* using a standard double-Gauss quadrature with the source introduced at $\mu = 1$. Both LD-**ONEDANT** results seem to have some difficulty at $\mu = 0$. This has been traced to the lack of a fixup mechanism for LD calculations. For a DD approximation with a set-to-zero fixup, (and for DGN = 96 and the source perpendicular given in column SDD96*), the discrepancy seems to have disappeared. Column RDD96 is included to show the standard **ONEDANT** result with linear interpolation between quadrature directions in order to obtain fluxes in the edit directions and for the source at the S_N direction closest to 1. The accuracy is greatly reduced for this case. Similar agreement is observed for the transmitted flux; however, flux fix-up caused oscillations for some cases at $\mu = 1$ and, as a result, no value was available. **MCNP** calculations, run for almost 2 weeks, are also included in the tables. At best only 3 digits of accuracy are obtained for the **MCNP** angular fluxes. This most likely results from a limitation of the current tally when angular fluxes are desired. The tally is subdivided into angular bins and the angular flux is the current in an angular bin divided by the average direction. Within each angular bin, it is not possible to use the actual directions for the divisor.

Table 2c shows the interior scalar flux comparison. Again excellent agreement is observed for the SLD200^{+} and SLD200* cases except near the surfaces. The **MCNP** results are not high precision because of an inherent limitation of the surface flux tally in slab geometry. Particles that intersect the surface flux tally surfaces at grazing angles activate this slight degradation in tally precision.

REFERENCES

[Benoist, 1996] P. Benoist, A. Kerchaff and R. Sanchez, Ann. Nucl. Ener., V23, 1033(1996).

[Case, 1953] K. Case, F. deHofman and G. Placzek, *Introduction to the Theory of Neutron Diffusion*, LASL report, (1953).

[Ganapol, 1998] B. Ganapol, Presentation at the 70^{th} birthday celebration for V.C. Boffi, Roma, April, 1998, in press, *TTSP*.

[Graves, 1972] P. R. Graves-Morris, Ed., Pade' Approximants, *IOP*, London, (1972).

[Inonu, 1970] E. Inonu, *Jour. Math Phys*., v11, 568(1970).

Table 1 Four-Slab Demonstration

Scalar Flux

x	err = 1.0e-05	Quad Order = 4
slab= 1		
0.00000E+00	1.34659E+00	1.34660E+00
2.00000E-01	1.45854E+00	1.45855E+00
4.00000E-01	1.51248E+00	1.51248E+00
6.00000E-01	1.53920E+00	1.53920E+00
8.00000E-01	1.54489E+00	1.54489E+00
1.00000E+00	1.50835E+00	1.50836E+00
slab= 2		
1.00000E+00	1.50837E+00	1.50836E+00
1.02000E+00	1.47672E+00	1.47672E+00
1.04000E+00	1.45601E+00	1.45599E+00
1.06000E+00	1.44165E+00	1.44162E+00
1.08000E+00	1.43386E+00	1.43387E+00
1.10000E+00	1.43881E+00	1.43881E+00
slab= 3		
1.10000E+00	1.43881E+00	1.43881E+00
1.90000E+00	1.38505E+00	1.38505E+00
2.70000E+00	1.14057E+00	1.14057E+00
3.50000E+00	8.78584E-01	8.78584E-01
4.30000E+00	6.32282E-01	6.32282E-01
5.10000E+00	3.72041E-01	3.72043E-01
slab= 4		
5.10000E+00	3.72045E-01	3.72043E-01
5.50000E+00	2.11853E-01	2.11853E-01
5.90000E+00	1.34346E-01	1.34346E-01
6.30000E+00	8.77821E-02	8.77822E-02
6.70000E+00	5.81507E-02	5.81507E-02
7.10000E+00	3.81154E-02	3.81155E-02

Table 2a Deep Penetration Problem: a=150mfp, L=10, ω=0.9

Table 2a: Reflection

μ	ANB	SLD200^{+}	RDD96	SDD96*	SLD200*	MCNP*
-1.0	0.439438	0.43943**6**	0.438**841**	0.439438	0.439438	--
-0.8	0.468676	0.468674	0.468577	0.468676	0.468676	0.4680
-0.6	0.491836	0.491832	0.492291	0.491836	0.491836	0.4922
-0.4	0.518433	0.518425	0.518452	0.518435	0.518435	0.5179
-0.2	0.499727	0.499710	0.500071	0.499727	0.499727	0.4995
0.0	0.395614	0.396395	0.397550	0.395614	0.396862	--

*Source at μ_0=1

+Lobatto quadrature

Table 2b Transmission x 10^{23}

μ	ANB	SLD200^{+}	RDD96	SDD96*	SLD200*	MCNP*
0.0	1.18640	1.18**868**	1.19**038**	--	1.19**007**	--
0.2	1.93253	1.932**46**	1.93**095**	1.932**43**	1.93253	1.93**63**
0.4	2.62817	2.62813	2.62**631**	2.628**03**	2.62815	2.63**30**
0.6	3.42320	3.423**16**	3.42**091**	3.423**02**	3.42318	3.42**67**
0.8	4.39503	4.394**98**	4.39**195**	4.394**79**	4.3949**9**	4.40**17**
1.0	5.63563	5.63555	5.62**665**	5.635**35**	5.63555	--

Table 2c Scalar Flux

x	ANB	SLD200^{+}	RDD96	SDD96*	SLD200*	MCNP*
0.05	1.54580	1.545**69**	1.546**64**	1.545**68**	1.545**69**	--
0.95	1.66667	1.6666**6**	1.667**15**	1.6666**6**	1.6666**6**	--
10.0	1.00460-01	1.00460	1.003**84**	1.00460	1.00460	1.004**8**
50.0	8.33981-08	8.3398**2**	8.33**326**	8.339**69**	8.3398**3**	8.34**22**
100.0	2.08521-15	2.08521	2.08**354**	2.085**14**	2.08521	2.08**64**
149.95	3.40420-23	3.403**92**	3.40**115**	3.403**77**	3.403**92**	--

CHAPTER IV

A NEW 1D-MULTIGROUP DISCRETE-ORDINATES ALGORITHM FOR NEUTRON TRANSPORT

1. INTRODUCTION

Simplicity and versatility are the hallmarks of the discrete ordinates (**SN**) numerical algorithm for neutron transport calculations. The method amounts to a convenient bookkeeping scheme for the neutron population as one sweeps in specified directions across a spatial domain. The method is generally considered one of brute force in that spatial and angular discretization is required. Therefore numerical errors resulting from discretizations are inherent in the method; and for this reason, the **SN** method has always been considered an approximate numerical scheme. The question naturally arises as to the possibility of constructing a fine-mesh multigroup **SN** approximation of similar or higher accuracy to a semi-analytical benchmark. If possible, then benchmark solutions could easily be generated and confidence in the **SN** method reinforced. In this presentation, a numerical variant of the **SN** algorithm will be devised in an attempt to eliminate both spatial and angular discretization errors and thus produce a truly accurate and converged numerical **SN** algorithm. The methodology couples a Romberg iterative strategy with a Wynn-epsilon acceleration to generate 4-and higher place accuracy for the group angular fluxes exiting and within a homogeneous slab medium. The Romberg iteration is based on knowledge of the spatial error induced by spatial discretization. Knowing that the error tail behaves like a power series in mesh spacing and by halving the mesh spacing and manipulating the tail, higher order terms can be eliminated. Thus, the solution can be made increasingly more accurate with relatively little effort. Wynn-epsilon (Wε) acceleration can then be applied to any quantity determined by the **SN** algorithm. The Wε acceleration is based on the Pade' approximant of an infinite series having the appropriate limit of a sequence of approximations and, though somewhat unpredictable, can be shown to be a most effective nonlinear accelerator.

We begin with a discussion of the two basic components of the new **MGCSN** algorithm. Next, the derivation of the algorithm is considered in full detail. It is noted that the approximate spatial nature of any 1D **SN** solution is determined by how the spatial integral over a mesh cell is to be approximated. This is a consequence of the inheritance of the integration

error by the solution itself. We conclude with a demonstration of the accuracy of the algorithm and several applications with relevant cross sections to assess algorithmic efficiency. Included is a discussion of how the **MGCSN** algorithm can be applied to critical systems.

2. THEORY

2.1. Romberg and Wynn-epsilon accelerations

A. Romberg Acceleration

The Romberg acceleration toward a limit [1], say of an algorithm based on a mesh spacing as the mesh spacing tends to zero, requires knowledge that the algorithm is of the form

$$A = A(h) + K_1 h^k + K_2 h^{k+1} + K_3 h^{k+2} + \ldots\ldots \qquad (1)$$

$A(h)$ is the numerical algorithm, h is the mesh spacing, K_j, j = 1,2,… are unknown coefficients and A is the exact limiting value as h tends to zero. For example, the following table indicates k for several well-known numerical

TABLE 1. EXAMPLES OF DISCRETE ALGORITHMS

Algorithm	$A(h)$	k
Trapezoidal Integration	$\frac{h}{2}\left[I_{j+1} + I_j\right]$	2
Simpson's Integration	$\frac{h}{2}\left[I_{j+1} + 2I_j + I_{j-1}\right]$	4
Forward Difference	$\frac{1}{h}\left[I_{j+1} - I_j\right]$	1
Central Difference	$\frac{1}{2h}\left[I_{j+1} - 2I_j + I_{j-1}\right]$	2

algorithms where $I_j \equiv I(x_j)$.

Consider the k^{th} order approximation of the form

$$A = A(h) + K_1 h^k + O\left(h^{k+1}\right), \qquad (2)$$

then for $h \to h/2$

$$A = A(h/2) + K_1 (h/2)^k + O\left(h^{k+1}\right); \qquad (3)$$

and through elimination of K_1, there results

$$A = B(h) + K_2 h^{k+1} + O\left(h^{k+2}\right) \qquad (4)$$

where a new more accurate algorithm has now been constructed of the form

$$B(h) \equiv \frac{2^k A(h/2) - A(h)}{2^k - 1} \ . \qquad (5)$$

Algorithm $B(h)$ is of order k+2. The elimination of K_j is continued until a desired order is reached. Note that Romberg acceleration is always initialized by the original numerical algorithm from which a more accurate approximation is to be obtained.

As an example, the following integral representation of the Henyey-Greenstein scattering kernel

$$f(\mu', \mu) =$$

$$= \frac{1-g^2}{2\pi} \int_0^{2\pi} d\phi \left\{ \frac{1}{\left[1 + g^2 - 2g\left(\mu'\mu + \sqrt{1-\mu'^2}\sqrt{1-\mu^2}\right)\cos(\phi)\right]^{3/2}} \right\} \qquad (6)$$

is to be evaluated to 9 places via the midpoint integration rule

$$\int_a^b dx g(x) = hg((a+b)/2) + K_1 h^2 + K_2 h^4 + \text{.....} \ . \qquad (7)$$

The evaluation is shown to be 9-place accuracy as anticipated. It is natural to then ask--Has the Romberg acceleration actually contributed to reducing the error that would have been present with the midpoint rule alone? To answer this question, the error of the original midpoint algorithm was determined. It was observed that the midpoint algorithm itself gives better than the desired accuracy. Therefore the additional Romberg acceleration was indeed not necessary for this case. Next, consider numerical differentiation. The numerical algorithm to be applied is the **C**omplex **S**tep **M**ethod (**CSM**) which gives the following evaluation for a derivative:

$$f'(x) = -\frac{1}{h}\mathrm{Im}[f(x+ih)] + K_1 h^2 + O\left(h^4\right). \qquad (8)$$

The **CSM** is to be applied to evaluate

$$\left.\frac{\partial f(\mu_0)}{\partial \mu'}\right|_{\phi=1.1\pi} =$$

$$= \frac{1-g^2}{2\pi}\frac{\partial}{\partial \mu'}\left\{\frac{1}{\left[1+g^2-2g\left(\mu'\mu+\sqrt{1-\mu'^2}\sqrt{1-\mu^2}\right)\cos(1.1\pi)\right]^{3/2}}\right\} \quad (9)$$

to 9-places. Again to address the necessity of the Romberg acceleration, the error associated with just the **CSM** was investigated. It was observed that at some points the relative error was as large as 10^{-3}. Thus, the Romberg acceleration is necessary to achieve the desired accuracy (10^{-9}) for this case. The Romberg acceleration will be applied to accelerate the inner sweeps of the standard **SN** algorithm.

B. Wynn-epsilon Acceleration

The Wynn-epsilon algorithm [2] is a nonlinear accelerator of a sequence

$$S_j, j = 1,2,.... \quad (10)$$

to its limit

$$S_\infty = \lim S_j . \quad (11)$$

The algorithm is the recurrence

$$\begin{aligned} \varepsilon_{-1}^{\ j} &\equiv 0 \\ \varepsilon_{0}^{\ j} &\equiv S_j \\ \varepsilon_{k+1}^{\ j} &= \varepsilon_{k-1}^{\ j+1} + \left[\varepsilon_{k}^{\ j+1} - \varepsilon_{k}^{\ j}\right]^{-1} \end{aligned} \quad (12)$$

that produces the following tableau:

$$\begin{array}{llllll} \varepsilon_{-1}^{\ 0} & \varepsilon_{0}^{\ 0} & \varepsilon_{1}^{\ 0} & \varepsilon_{2}^{\ 0} & \ddots & \\ \varepsilon_{-1}^{\ 1} & \varepsilon_{0}^{\ 1} & \varepsilon_{1}^{\ 1} & \ddots & & \\ \varepsilon_{-1}^{\ 2} & \varepsilon_{0}^{\ 2} & \ddots & & & \\ \varepsilon_{-1}^{\ 3} & \ddots & & & & \\ \ddots & & & & & \end{array} \quad (13)$$

The diagonal elements, indicated by the arrow, are interrogated for convergence.

While it is beyond the scope of this presentation to derive the Wε algorithm, it can be motivated from the following analysis. Let c_n be the forward difference

$$c_{n+1} \equiv S_{n+1} - S_n . \tag{14}$$

Next, form the power series

$$f(z) \equiv \sum_{n=0}^{\infty} c_n z^n \tag{15a}$$

which has the desired limit

$$f(1) = S_\infty . \tag{15b}$$

It is now possible to approximate the power series by a Pade' approximant

$$f(z) = [L/M](z) + O\left(z^{L+M+1}\right) \tag{16}$$

where

$$[L/M] \equiv \frac{a_0 + a_1 z + \ldots + a_L z^L}{b_0 + b_1 z + \ldots + b_L z^L} . \tag{16a}$$

Finally it can be shown [2] that the diagonal of the tableau is the k/k Pade' approximant

$$\varepsilon_{2k}^0 = [k/k](1). \tag{17}$$

The Wε algorithm will be tested on the following Legendre polynomial expansion:

$$h(\mu', \mu) = \frac{1}{2} \sum_{l=0}^{\infty} g^l P_l(\mu') P_l(\mu) \tag{18}$$

where the sequence of partial sums,

$$S_j(\mu', \mu) = \frac{1}{2} \sum_{l=0}^{j} g^l P_l(\mu') P_l(\mu), \tag{19}$$

is to be accelerated to its limit. Table 2 shows the progression toward the limit for $\mu' = 1$, $\mu = 1$,and g = 0.999. Iterations from 1 to 30 and 62 to 92 are shown. The Wε accelerated value, the original partial sum and the error of the Wε value are indicated. The Wε algorithm is applied using only the last 5 iterates for prediction. This is done to avoid using initial terms that are known to be inaccurate. Observing the original sequence shows only a mild trend at best toward the limit. In contrast, the Wε entries shows 3- to 4-place

convergence after 30 iterations with continued remarkable progress to 5- or 6- place terms after 90 iterations. This demonstration indicates how efficient the Wε acceleration can be. A smoother approach to the limit can be achieved if more iterates are taken for prediction. The Wε algorithm will be applied to the inner iterations of the **SN** algorithm and to the outer angular quadrature iteration.

3. DERIVATION OF THE MGCSN ALGORITHM

3.1. Transport Setting

We begin with the usual multigroup neutron transport equation

$$\left[\mu \underline{I}\frac{\partial}{\partial x}+\underline{\Sigma}\right]\vec{\phi}(x,\mu)=\frac{1}{2}\left[\underline{\Sigma}_S+\vec{\chi}\underline{\Sigma}_f^T\underline{\nu}\right]\vec{\phi}(x) \qquad (20a)$$

where

$$\vec{\phi}(x,\mu)\equiv\begin{bmatrix}\phi_1\\ \phi_2\\ ....\\ \phi_G\end{bmatrix}, \qquad \vec{\phi}(x)\equiv\int_{-1}^{1}d\mu\vec{\phi}(x,\mu) \qquad (20b)$$

$$\vec{\chi}\equiv\begin{bmatrix}\chi_1\\ \chi_2\\ ....\\ \chi_G\end{bmatrix}, \qquad \vec{\Sigma}_f\equiv\begin{bmatrix}\Sigma_1\\ \Sigma_2\\ ....\\ \Sigma_G\end{bmatrix} \qquad (20c)$$

$$\underline{\nu}\equiv diag\left[\nu_g, g=1,2,...G\right], \qquad \underline{\Sigma}\equiv diag\left[\Sigma_g, g=1,2,...G\right]. \qquad (20d)$$

Isotropic scattering has been assumed in each of the G groups for a slab of width a. A (plane) beam source in group s in direction μ_0 impinges on the left face and vacuum borders the right face for all groups giving the following boundary conditions:

$$\begin{aligned}\vec{\phi}(0,\mu)&=\vec{e}_s\delta(\mu-\mu_0), \quad \mu>0\\ \vec{\phi}(a,\mu)&=\vec{0}, \qquad\qquad\quad \mu<0\end{aligned} \qquad (20e)$$

with

$$\vec{e}_S \equiv \begin{bmatrix} 0 \\ 0 \\ .... \\ 1_S \\ .... \\ 0 \end{bmatrix} . \qquad (20f)$$

The medium is composed of fissionable material and is assumed to be subcritical.

The most straightforward approach is to partition the flux into an uncollided and collided contribution which satisfies

$$\begin{aligned} &\left[\mu \underline{I} \frac{\partial}{\partial x} + \underline{\Sigma}\right]\vec{\phi}_0(x,\mu) = \vec{0} \\ &\vec{\phi}(0,\mu) = \vec{e}_S \delta(\mu - \mu_0), \quad \mu > 0 \\ &\vec{\phi}(a,\mu) = \vec{0}, \qquad\qquad \mu < 0 \end{aligned} \qquad (21a)$$

and whose solution is

$$\vec{\phi}_0(x,\mu) = \vec{e}_S \delta(\mu - \mu_0) e^{-\Sigma_g x/\mu} \Theta(x/\mu) . \qquad (21b)$$

The uncollided contribution leads to a first collided scattering source of the form

$$\begin{aligned} \vec{q}_1(x) &\equiv \frac{1}{2}\underline{\Sigma}_S \int_{-1}^{1} d\mu \vec{\phi}_0(x,\mu) \\ &= \frac{1}{2}\underline{\Sigma}_S e^{-\Sigma_g x/\mu_0} \vec{e}_S \Theta(x/\mu_0) \end{aligned} \qquad (22)$$

The collided contribution therefore satisfies

$$\begin{aligned} &\left[\mu \underline{I} \frac{\partial}{\partial x} + \underline{\Sigma}\right]\vec{\phi}_c(x,\mu) = \frac{1}{2}\left[\underline{\Sigma}_S + \vec{\chi}\underline{\Sigma}_f^T \underline{\nu}\right]\vec{\phi}_c(x) + \vec{q}_1(x) \\ &\vec{\phi}_c(0,\mu) = \vec{0}, \quad \mu > 0 \\ &\vec{\phi}_c(a,\mu) = \vec{0}, \quad \mu < 0 \end{aligned} \qquad (23)$$

which will be to focus of the **MGCSN** method.

Table 2 Demonstration of Wε Acceleration
Henyey-Greenstein: $\mu' = 1,\ \mu = 0.9,\ g = 0.999$

j	$S_j(W\varepsilon)$	S_j	$e(W\varepsilon)$	j	$S_j(W\varepsilon)$	S_j	$e(W\varepsilon)$
0	**5.0000E-01**	**5.0000E-01**	**1.5540E+78**	62	1.1182E+00	1.2176E+00	2.6251E-05
1	**9.4955E-01**	**9.4955E-01**	**4.7343E-01**	63	1.1182E+00	1.1527E+00	4.7513E-05
2	**1.3063E+00**	**1.3063E+00**	**2.7312E-01**	64	1.1183E+00	1.0822E+00	1.0615E-04
3	**1.5419E+00**	**1.5419E+00**	**1.5276E-01**	65	1.1185E+00	1.0201E+00	1.3965E-04
4	**1.6454E+00**	**1.6454E+00**	**6.2934E-02**	66	1.1187E+00	9.7859E-01	1.4370E-04
5	8.1117E-01	1.6250E+00	1.0285E+00	67	1.1188E+00	9.6560E-01	1.1985E-04
6	9.1760E-01	1.5051E+00	1.1598E-01	68	1.1189E+00	9.8320E-01	7.4702E-05
7	9.9448E-01	1.3225E+00	7.7311E-02	69	1.1189E+00	1.0274E+00	1.8443E-05
8	1.0497E+00	1.1193E+00	5.2568E-02	70	1.1189E+00	1.0890E+00	3.7281E-05
9	1.0890E+00	9.3616E-01	3.6127E-02	71	1.1188E+00	1.1555E+00	8.1739E-05
10	1.1161E+00	8.0590E-01	2.4289E-02	72	1.1187E+00	1.2136E+00	1.0721E-04
11	1.1329E+00	7.4843E-01	1.4838E-02	73	1.1185E+00	1.2519E+00	1.1020E-04
12	1.1408E+00	7.6856E-01	6.9202E-03	74	1.1184E+00	1.2632E+00	9.1732E-05
13	1.1416E+00	8.5631E-01	6.7887E-04	75	1.1184E+00	1.2456E+00	5.6784E-05
14	1.1376E+00	9.8982E-01	3.4990E-03	76	1.1183E+00	1.2030E+00	1.3165E-05
15	1.1313E+00	1.1401E+00	5.6077E-03	77	1.1184E+00	1.1442E+00	3.0106E-05
16	1.1245E+00	1.2771E+00	6.0562E-03	78	1.1185E+00	1.0813E+00	6.4655E-05
17	1.1185E+00	1.3749E+00	5.3639E-03	79	1.1185E+00	1.0266E+00	8.4396E-05
18	1.1140E+00	1.4169E+00	3.9666E-03	80	1.1186E+00	9.9106E-01	8.6530E-05
19	1.1116E+00	1.3978E+00	2.2275E-03	81	1.1187E+00	9.8133E-01	7.1789E-05
20	1.1110E+00	1.3247E+00	4.9475E-04	82	1.1188E+00	9.9903E-01	4.4056E-05
21	1.1120E+00	1.2143E+00	9.2178E-04	83	1.1188E+00	1.0402E+00	9.4718E-06
22	1.1141E+00	1.0901E+00	1.8319E-03	84	1.1188E+00	1.0965E+00	2.4838E-05
23	1.1165E+00	9.7697E-01	2.1984E-03	85	1.1187E+00	1.1563E+00	5.2223E-05
24	1.1189E+00	8.9654E-01	2.0943E-03	86	1.1186E+00	1.2078E+00	6.7810E-05
25	1.1207E+00	8.6320E-01	1.6414E-03	87	1.1185E+00	1.2410E+00	6.9314E-05
26	1.1218E+00	8.8159E-01	9.7963E-04	88	1.1185E+00	1.2493E+00	5.7283E-05
27	1.1221E+00	9.4608E-01	2.5730E-04	89	1.1184E+00	1.2315E+00	3.4812E-05
28	1.1217E+00	1.0423E+00	3.8484E-04	90	1.1184E+00	1.1916E+00	6.8412E-06
29	1.1207E+00	1.1501E+00	8.4200E-04	91	1.1185E+00	1.1376E+00	2.0877E-05
30	1.1195E+00	1.2481E+00	1.0647E-03	92	1.1185E+00	1.0805E+00	4.2957E-05

3.2. The MGCSN Method

Since the scattering is assumed to be isotropic, a straightforward collocation can be used for angular discretization. Here, we use the Double Gauss quadrature

$$\mu \equiv \left\{ \pm \mu_m ; P_N \left(2\left|\mu_m\right| - 1 \right) = 0, \quad m = 1, 2N \right\} \tag{24}$$

as the discrete directions giving

$$\begin{aligned} &\left[\mu_m \underline{I} \frac{\partial}{\partial x} + \underline{\Sigma} \right] \vec{\phi}_{cm}(x) = \\ &\quad = \frac{1}{2} \left[\underline{\Sigma}_S + \vec{\chi} \underline{\Sigma}_f^T \underline{\nu} \right] \sum_{m'=1}^{2N} \omega_{m'} \vec{\phi}_{cm'}(x) + \vec{q}_1(x) \end{aligned} \tag{25a}$$

where ω_m are the quadrature weights. The *m*-subscript represents the angular discretization with

$$\vec{\phi}_{cm}(x) \equiv \vec{\phi}_c\left(x, \mu_m\right). \tag{25b}$$

To arrive at a spatial discretization, we first uniformly discretize the slab width into mesh cells of size *h* and then integrate eq(25a) over a mesh cell

$$\begin{aligned} &\mu_m \left[\vec{\phi}_{cm,\, j+1} - \vec{\phi}_{cm,\, j} \right] + \underline{\Sigma} \int_h dx \vec{\phi}_{cm}(x) = \\ &\quad = \frac{1}{2} \left[\underline{\Sigma}_S + \vec{\chi} \underline{\Sigma}_f^T \underline{\nu} \right] \sum_{m'=1}^{2N} \omega_{m'} \int_h dx \vec{\phi}_{cm'}(x) + \int_h dx \vec{q}_1(x) \end{aligned} \tag{26}$$

The *j*-subscript represents the flux at the interval edges. If we were to follow common practice, the integral of the flux over interval *h* would be related to the interval edge fluxes in some way. Usually, the integral is considered to be the cell centered flux and is related to the edge flux by a simple average. This is the well-known diamond difference approximation. Here, we adopt a more general view where the integration is interpreted as a quadrature approximation of a given order *k*

$$\int_h dx \vec{\phi}_{cm}(x) = \bar{\bar{I}}(h) + K_1 h^k + K_2 h^{k+1} + K_3 h^{k+2} + \ldots\ldots \tag{27}$$

where $\bar{\vec{I}}(h)$ is the quadrature rule. Note the connection to the Romberg algorithm. The integration over the source is explicit

$$\int_h d\vec{x}\vec{q}_1(x) = \frac{\mu_0}{2}\underline{\Sigma}_s\vec{e}_s\left[e^{-\underline{\Sigma}x_j/\mu_0} - e^{-\underline{\Sigma}x_{j+1}/\mu_0}\right] \equiv \vec{U}_{js}. \qquad (28)$$

Since the quadrature over the interval is the sole spatial approximation, the desired solution will also possess the same form of the error tail. In particular

$$\vec{\phi}_{cm,j} = \bar{\vec{\phi}}_{cm,j} + \alpha_1 h^k + \alpha_2 h^{k+1} + \alpha_3 h^{k+2} + \ldots\ldots \qquad (29)$$

where $\bar{\vec{\phi}}$ is the **SN** approximation. If a trapezoidal rule is assumed, then *k* is 2 and

$$\bar{\vec{I}}(h) \equiv \frac{h}{2}\left[\vec{I}_{j+1} + \vec{I}_j\right];$$

and the "diamond difference" approximation emerges (the over bar is suppressed)

$$\left[\mu_m\underline{I} + \frac{h}{2}\left(\underline{\Sigma} - \frac{\omega_m}{2}\underline{\Sigma}_s\right)\right]\vec{\phi}_{cm,j+1} - \left[\mu_m\underline{I} - \frac{h}{2}\left(\underline{\Sigma} - \frac{\omega_m}{2}\underline{\Sigma}_s\right)\right]\vec{\phi}_{cm,j} = \qquad (30)$$
$$= \frac{h}{4}\left[\underline{\Sigma}_s + \vec{\chi}\underline{\Sigma}_f^T\underline{\nu}\right]\sum_{m'=1}^{2N}\omega_{m'}\left[\vec{\phi}_{cm,j+1} + \vec{\phi}_{cm,j}\right] + \vec{U}_{js}.$$

But more importantly, any integration rule can be put in place with a higher error order for more accuracy. With the trapezoidal rule, we know the order of the error ($k = 2$) and the form of the error tail of the solution is given by eq(27). With this knowledge, a Romberg iterative scheme can be applied to eq(27) to successively eliminate higher order error terms. This is an extension of Richardson's extrapolation as applied previously to the transport equation [3].

Thus, the **SN** algorithm serves as the basis for the Romberg algorithm. Transport sweeps with source iteration are performed in the usual manner, for $\mu \geq 0$

$$\vec{\phi}_{cm,j+1} = \left[\underline{T}_m^+\right]^{-1}\underline{T}_m^-\vec{\phi}_{cm,j} +$$
$$+ \frac{h}{4}\left[\underline{T}_m^+\right]^{-1}\left[\underline{\Sigma}_s + \vec{\chi}\underline{\Sigma}_f^T\underline{\nu}\right]_{m'=1\neq m}\sum^{N}\omega_{m'}\left[\vec{\phi}_{cm,j+1} + \vec{\phi}_{cm,j}\right] + \left[\underline{T}_m^+\right]^{-1}U_{js}. \qquad (31a)$$

for $\mu < 0$

$$\vec{\phi}_{cm,j} = \left[\underline{T}\bar{m}\right]^{-1} \underline{T}\bar{m}^{+}\vec{\phi}_{cm,j+1} -$$
$$-\frac{h}{4}\left[\underline{T}\bar{m}\right]^{-1}\left[\underline{\Sigma}_s + \vec{\chi}\underline{\Sigma}_f^T \underline{\nu}\right]\sum_{m'=1\neq m}^{N} \omega_{m'}\left[\vec{\phi}_{cm,j+1} + \vec{\phi}_{cm,j}\right] + \left[\underline{T}\bar{m}\right]^{-1} U_{js}. \tag{31b}$$

where

$$\underline{T}\bar{m}^{\pm} \equiv \left[\mu_m \underline{I} \pm \frac{h}{2}\left(\underline{\Sigma} - \frac{\omega_m}{2}\underline{\Sigma}_s\right)\right].$$

To accelerate the convergence of the inner iterations, Wε acceleration can be applied since the inner iterations should tend to a limit.

The final element of the **MGCSN** method is an attempt to converge in the angular quadrature order. This is seldom if ever included as a standard feature in an **SN** code. The order *N* of the angular approximation is increased until convergence with convergence accelerated through the Wε accelerator. The Wε scheme uses only the last 5 Romberg converged values for prediction. More Romberg converged iterates could be used, but it is felt that the last 5 values are the most accurate.

Thus, with both acceleration algorithms, there is no guessing as to which is the proper quadrature order or spatial discretization to use; and true algorithmic convergence can eventually be reached for most cases.

3.3. Flow Diagram Summary of the MGCSN Algorithm

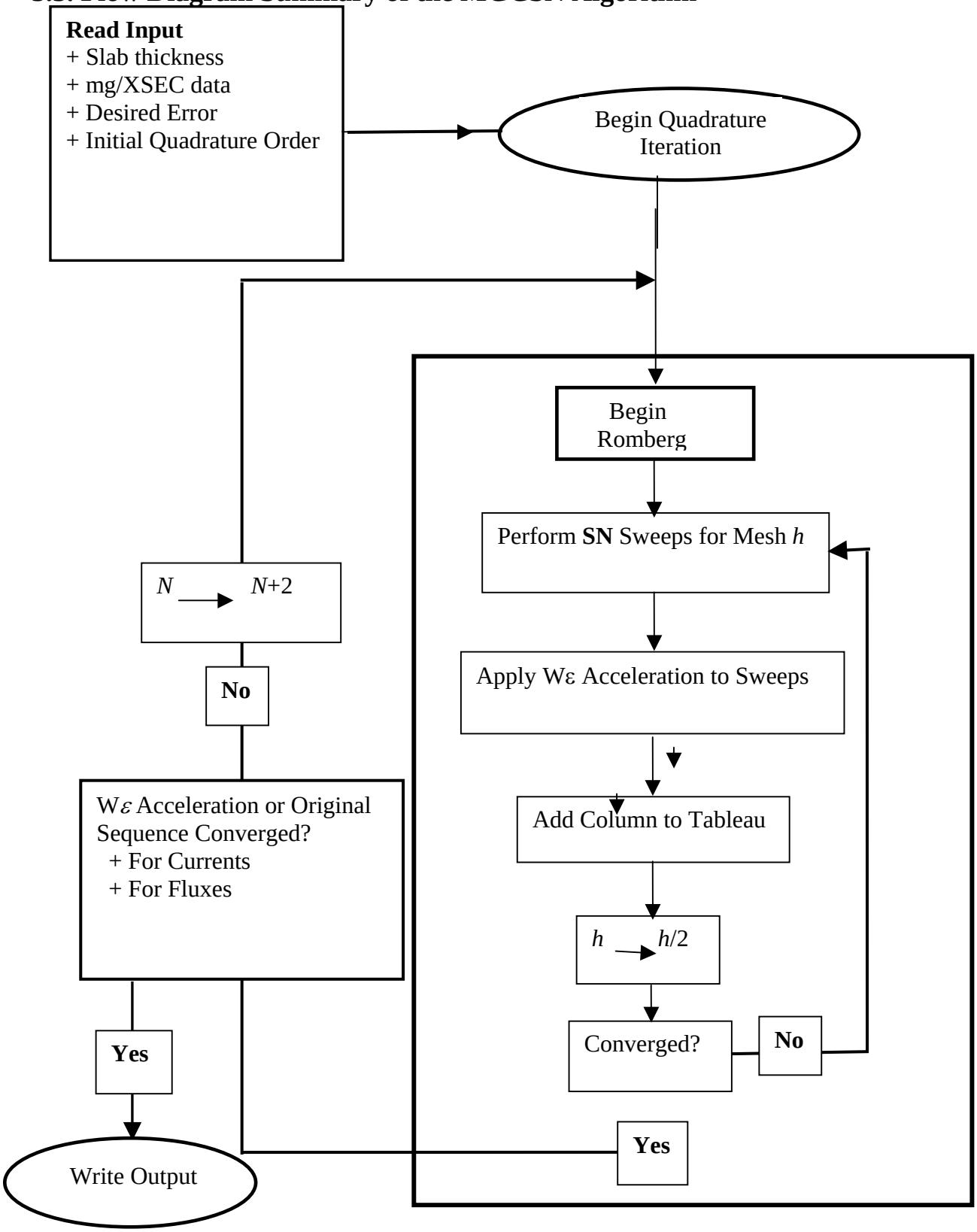

4. DEMONSTRATION

4.1. Convergence Trends

As a demonstration of the convergence of the **CSN** method in the one group approximation, various relative error scenarios for the exiting current at the source surface

$$R_f \equiv \int_0^1 d\mu \mu \phi(0,\mu) \qquad (32)$$

have been determined for a perpendicular source striking a slab of 2*mfp* thickness and 0.95 number of secondaries. The relative errors are plotted as scatter curves in Fig.1. Since **SN** calculations are required to specify each level of the Romberg tableau for a given quadrature order *N*, the relative error associated just with the last two **SN** calculations at convergence of the Romberg acceleration is displayed as the hexagonal (light green) symbol scatter plot. This provides one measure of an unaccelerated result. Apparently, no better than about 6 digit agreement (10^{-6} relative error) between **SN** iterates is possible independently of the **SN** order. The Romberg converged value also agrees with the **SN** value to about 6 digits as shown as the hexagonal symbol scatter plot (dark red/white) but may possess more accuracy as we shall see. The Romberg iteration typically converged at 512 or 1024 spatial intervals. Next, we examine the variation of the relative error of the **SN** calculation at the smallest mesh (when the Romberg acceleration has converged) with quadrature order *N* as shown by the diamond (pink) scatter plot. As seems evident, excellent convergence to about 10^{-10} error is achieved just with the **SN** algorithm alone. However one must be cautioned since this measure only compares **SN** to **SN** and not to the converged Wε value, which is supposedly the correct one. In particular, 10 digit agreement does not necessarily mean that they are all the correct digits. When **SN** values are compared to the converged Wε values given by the (red) square scatter plot, it is observed that the **SN** values have saturated and indeed are not at a 10^{-10} error, but at 10^{-7} accuracy. In comparing just the relative error of the Romberg converged values (green triangle scatter plot), a significant decrease in error is observed with quadrature order indicating the power of the Romberg algorithm. To verify that the converged Romberg values are indeed near the true result, their relative error with respect to the Wε values is shown as the black circle scatter plot which exhibits a similar downward trend. The advantage of the Wε algorithm is realized when the relative error of successive Wε values (blue triangle) is compared to the previous scatter plot. Using the Wε algorithm reduces (in a somewhat

erratic way) the relative error by a factor of about 10 to its lowest value. Thus, it can be concluded that the error reduction in the reflectance would not be possible without the application of the two acceleration schemes together.

4.2. Comparison to a Semi-Analytical Benchmark

As a second demonstration, again consider the slab of width 2*mfp* in the one group approximation as above and determine the transmittance

$$T_n \equiv \int_0^1 d\mu \mu \phi(a, -\mu) \tag{33}$$

as well as the reflectance to a relative error of 10^{-10}. In the last section, it was supposed that the Wε converged value was the correctly converged value. This conjecture could easily be contested however without additional proof. Recall that if the Romberg and Wε schemes had not been applied, one would have concluded that the **SN** algorithm itself converged to 10 places as *N* was increased to 50 with 512 intervals. Only after comparison with the Wε algorithm would this conclusion be shown false. But is the Wε value the truly converged value? One way to gain some confidence is through comparison to an equally accurate value. Fortunately, the **BLUE** code [4] exists which can be made to produce such accuracy. The **BLUE** code is based on the **G**reen's **F**unction **M**ethod, which in a rather involved mathematical procedure to generate an analytical representation of the flux using the Green's function and Placzek's lemma—a very different method from the **CSN** algorithm.

A comparison of the Wε and **BLUE** values and the most accurate **SN** values is shown in Table 3. The accuracy of the Wε values is confirmed (at least for this case). From experience with analytical benchmarking, it is the conclusion of the author that this confirmation will also hold for the multi-(few) group case. Thus, the relatively unsophisticated **CSN** bookkeeping algorithm can be made to give highly accurate benchmark results with significantly less computational effort than a semi-analytical benchmark.

Table 3 Benchmark Comparison

Method	R_f	T_n
GFM	4.287236043e-01	4.093083959e-01
CSN:*N/Lx*:44/1024	4.287236043e-01	4.093083959e-01
SN:*N/Lx*:44/1024	4.287235412e-01	4.093084747e-01

In Fig. 2, the **CSN** and **BLUE** scalar fluxes are compared. The **CSN** scalar flux is not an accelerated value but that of the most accurate **SN** calculation. Provision will eventually be made for converged angular and scalar fluxes.

4.3 Some Multigroup Demonstrations

As a test of the full **MGCSN** method several one group and few group examples will be presented. Here, the intent is only to demonstrate consistent and reasonable results can be obtained and not to demonstrate the limits of the method. All cases considered are found in the excellent benchmark compilation of eigenvalue benchmarks published by Sood, Forester and Parsons [5].

A. One-group

The nuclear properties of the materials for the one group cases considered are contained in Table 4.

Table 4 One Group Nuclear Parameters

Material	ν	$\Sigma_f(cm^{-1})$	$\Sigma_s(cm^{-1})$	$\Sigma_t(cm^{-1})$	$2r_c(cm)$
Pu239	2.84	0.0816	0.225216	0.32640	4.513502
U235	2.70	0.06528	0.248064	0.32640	5.745869

The first example is for a bare plutonium slab of thickness 2cm which is well below the critical thickness. **CSN** will be run in the decoupled multigroup mode. In this mode, each group represents a one group calculation decoupled from all the others. In this way, many multigroup cases can be accommodated in a single **MGCSN** run. Figure 3, shows the variation of the scalar flux across the slab when the scattering cross section is reduced with all other parameters fixed. A reduction of the flux results as the scattering cross section is reduced because of the increased absorption as would be expected.

Unfortunately, there are no published values with which to compare the **CSN** results but there is a sanity check involving criticality that can be applied that provides some confirmation of proper algorithmic operation. Since the critical thickness of the slab for the given parameters is known, one might ask --What happens when a fixed source steady state computation is applied to a critical system? If the calculation is performing properly, some indication of physical incompatibility should emerge. This conjecture

will now be tested by varying the fission cross section through the value that gives criticality ($\Sigma_{fc} = 0.0816$) for a bare PU slab

$$\Sigma_f = 0.07, 0.08, 0.08159, 0.08161, 0.09.$$

Figure 4 shows the resulting scalar flux through criticality indicating nothing at all unusual. The flux seems to increase with no unphysical behavior. However, observing the exiting currents shown in Table 5a, indicates unphysical negative values on the high side of criticality. When the appro-

Table 5a Pu Near Criticality

Σ_f	R_f	T_n
0.07	6.5530E-01	8.2988E-01
0.08	4.8387E+00	5.0051E+00
0.08159	7.7541E+02	7.7558E+02
0.08161	-7.7566E+02	-7.7549E+02
0.09	-9.2603E-01	-7.6920E-01

ach is refined, the unphysical values persist as shown in Table 5b. If the current showed unphysical behavior, why was this not also shown in the

Table 5b Pu Near Criticality (refined)

Σ_f	R_f	T_n
0.081598	3.8733E+03	3.8735E+03
0.081599	7.7378E+03	7.7380E+03
0.081601	-7.7031E+03	-7.7028E+03
0.081602	-3.8818E+03	-3.8816E+03
0.081603	-2.5870E+03	-2.5868E+03

scalar flux? The reason is that the scalar flux is not derived from converged angular fluxes but from the most accurate values of the **SN** calculation. Remarkably, criticality is sensed only after the application of the Romberg and Wynn-epsilon accelerations. To verify this Table 5c shows converged values of the angular flux at the first and last quadrature directions. The unphysical behavior is now evident.

To see that the apparent indication of criticality by the **CSN** method is not a fortuitous occurrence, the same analysis was performed on a bare U235 slab

Table 5c Angular Flux

Σ_f	$\phi(0,1)$	$\phi(\alpha,N)$
0.07	1.1591E+00	1.0997E+00
0.08	8.7190E+00	8.6506E+00
0.08159	1.4046E+03	1.4046E+03
0.08161	-1.4052E+03	-1.4052E+03
0.09	-1.7079E+00	-1.7869E+00

Table 5d U235 Near Criticality

Σ_f	R_f	T_n
0.05	4.0746E-01	4.9122E-01
0.06	1.1750E+00	1.2469E+00
0.06527	6.1424E+02	6.1430E+02
0.06529	-6.1283E+02	-6.1277E+02
0.07	-1.2784E+00	-1.2208E+00

(Σ_{fc} = 0.06528) as shown in Table 3d with the identical outcome around the critical fission cross section.

From this investigation, we can conclude that the **CSN** method is sensitive to criticality through its accelerations—an interesting result indeed!

B. Two-groups

The 2-group bare Pu239 slab is considered next (Problem 45 in [5]). Figure 5 shows the two-group fluxes for sources alternately in each group. The expected symmetry is observed.

D. Six-groups

The final case considered is for six groups. A special cross section set has been devised and is found in Tables 59-64 in reference 5. The set is constructed such that there is possible down or up scatter to two adjacent groups and groups [1,6], [2,5], [3,4] are equivalent. Therefore, for symmetrically placed sources within the group structure, symmetrical results in energy are expected. This is seen to be the case for a 2cm thick slab as shown in Fig. 6 where the corresponding groups fall on top of each other.

The **MGCSN** method can also be used to predict the critical thickness for

Table 6a Subcritical for a =6.35cm

Gp	R_f	T_n
1	1.6982E+02	1.6963E+02
2	4.8900E+01	4.8684E+01
3	9.3814E+00	9.3474E+00
4	9.3814E+00	9.3474E+00
5	4.8900E+01	4.8684E+01
6	1.6982E+02	1.6963E+02

Table 6b Supercritical for a =6.36cm

Gp	R_f	T_n
1	-2.6026E+02	-2.6046E+02
2	-7.4533E+01	-7.4756E+01
3	-1.4322E+01	-1.4357E+01
4	-1.4322E+01	-1.4357E+01
5	-7.4533E+01	-7.4756E+01
6	-2.6026E+02	-2.6046E+02

this case. As shown in Tables 6, positive and negative exiting currents are given by a = 6.35 and 6.36 respectively. If two additional cases are run and the reciprocal of the reflectance for groups 1,2 and 3 is plotted against a, Fig. 7 results which seems to most remarkably pinpoint the critical thickness if it is assumed to occur at infinite flux. At this point, the determination of the critical thickness is conjecture; however, verification is planned.

5. CONCLUSIONS AND FUTURE EFFORT

In this presentation, only the fundamentals of the **MGCSN** method have been given. There remain several issues that must be addressed after which the **MGCSN** method could possibly be viewed as one of the most effective methods for generating highly accurate 1D transport solutions ever devised. As shown, the numerical solution retains the simplicity of the **SN** algorithm and with little extra effort can be made to render semi-analytical benchmark quality solutions. The algorithm is built around two powerful acceleration techniques that enable sequences to reach their limits most efficiently. The accuracy of the method has been demonstrated as well its application to few group cases.

Still, however, there are some unanswered questions such as:

+ How can fluxes be obtained at specific spatial edit points?
+ Can **DSA** be incorporated into the inner iteration strategy to further speedup the computation?
+ How does the algorithm fair for anisotropic scattering?
+ Can **CSN** be coupled to a numerical Laplace transform inversion to generate time dependent results?
+ Does a **CSN/GFM** hybrid make sense?
+ What about multidimensions?

These and other issues will be addressed as the **MGCSN** method matures through application.

REFERENCES

[1] Press, W.H.; Flannery, B.P.; Teukolsky, S.A.; and Vetterling, W.T. "Romberg Integration." §4.3 in *Numerical Recipes in FORTRAN: The Art of Scientific Computing, 2nd ed.* Cambridge, England: Cambridge University Press, pp. 134-135, (1992).

[2] G. A. Baker and P. Graves-Morris, *Pade' Approximants*, Cambridge University Press, NY, 1996.

[3] E. Allen, Richardson Extrapolation to the Transport Equation, NSE **99**,123-132(1988).

[4] B. Ganapol and K. Parsons, M&C Topical Mtg., *A Heterogeneous Analytical Benchmark*, Madrid Spain,1999.

[5] A. Sood, A Forester and D.K. Parsons, Analytical Benchmark Test Set for Criticality Code Verification, *Progress in Nuclear Energy*, 42,55-106, (2003).

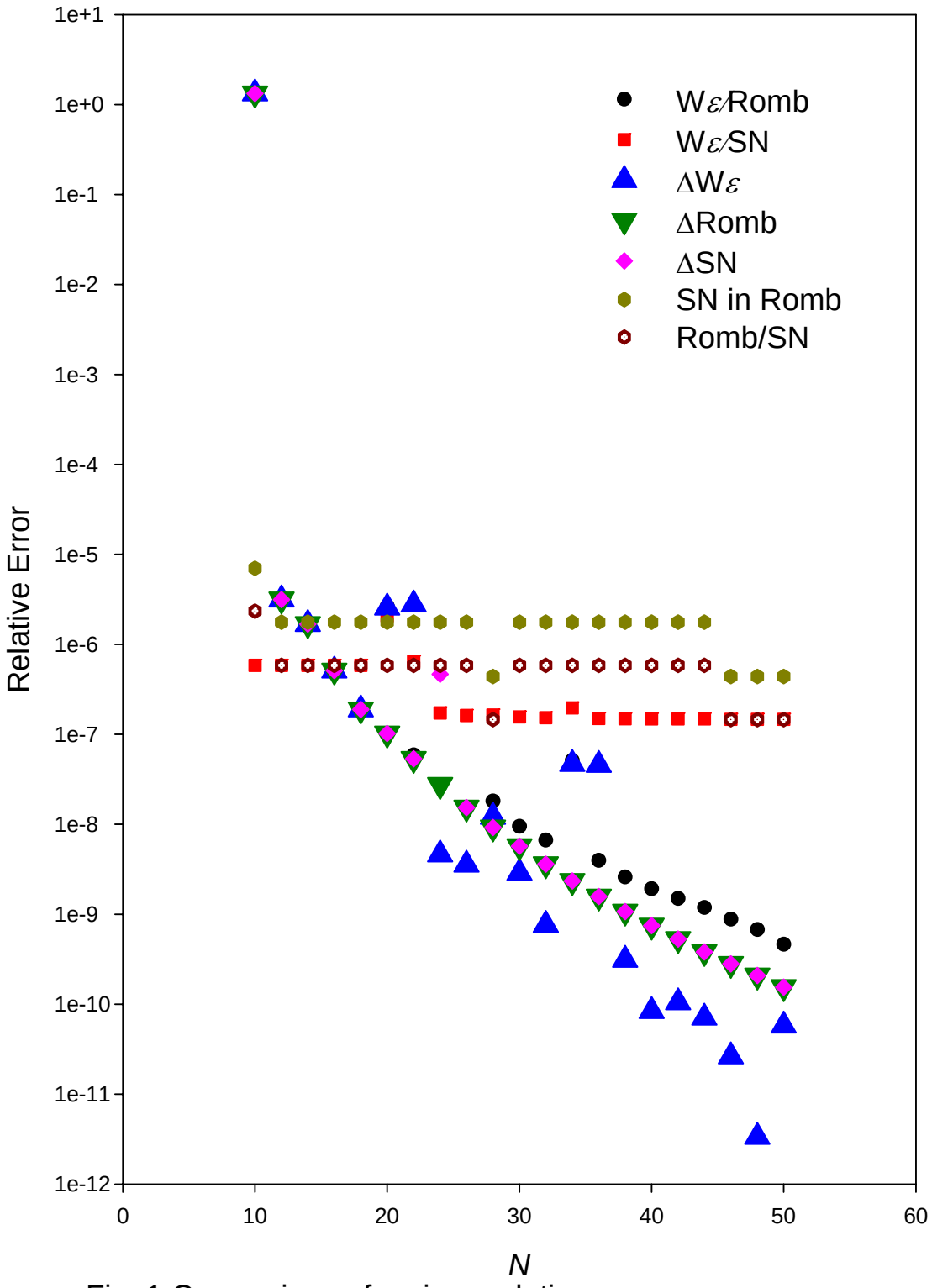

Fig. 1 Comparison of various relative errors

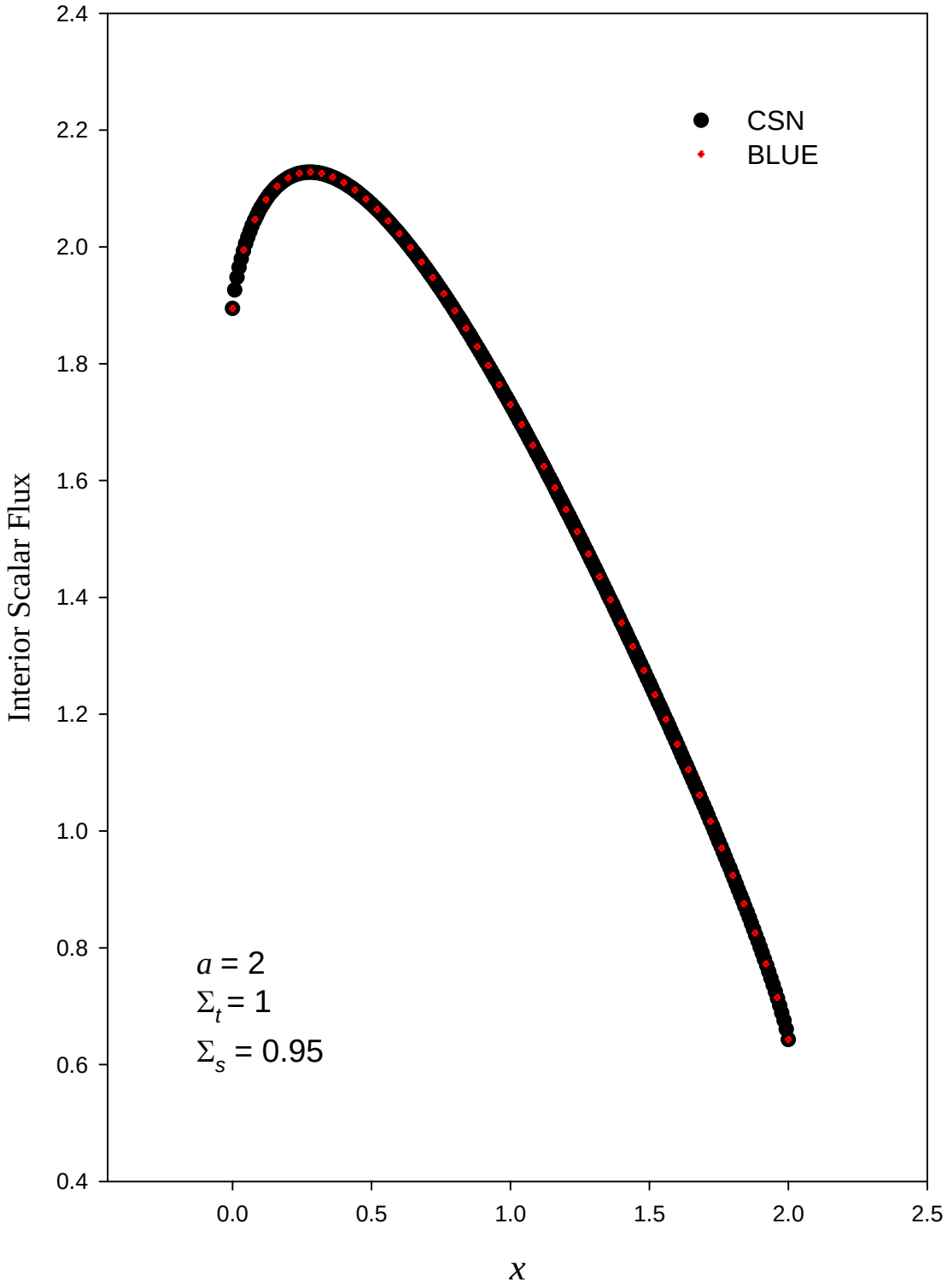

FIg.2 Comparision to the **BLUE** analytical benchmark

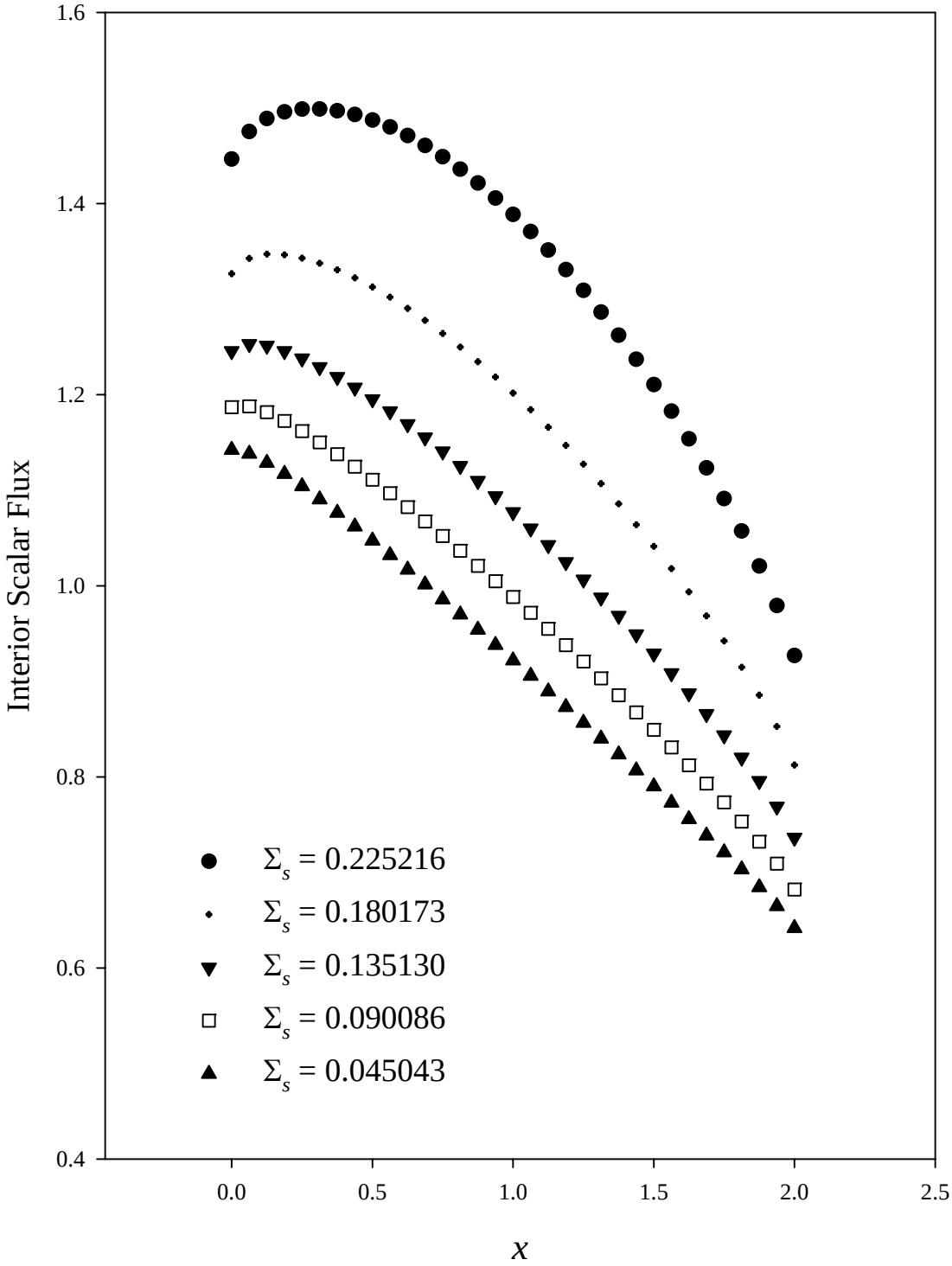

Fig. 3 Variation of Σ_s for Pu239 with $a = 2$ and $\Sigma_t = 0.32640$

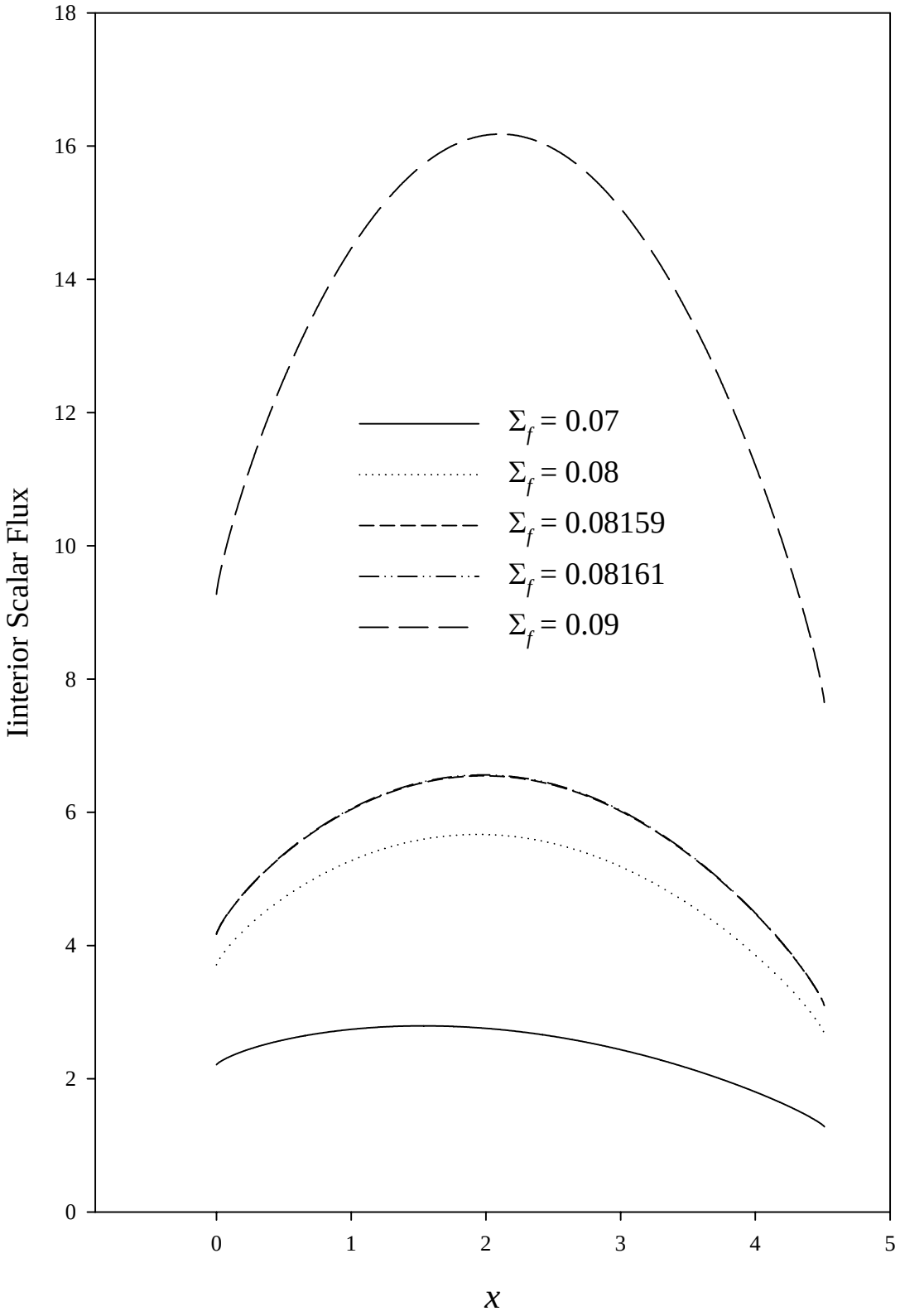

Fig. 4 SN scalar fluxes for Pu239 through critical

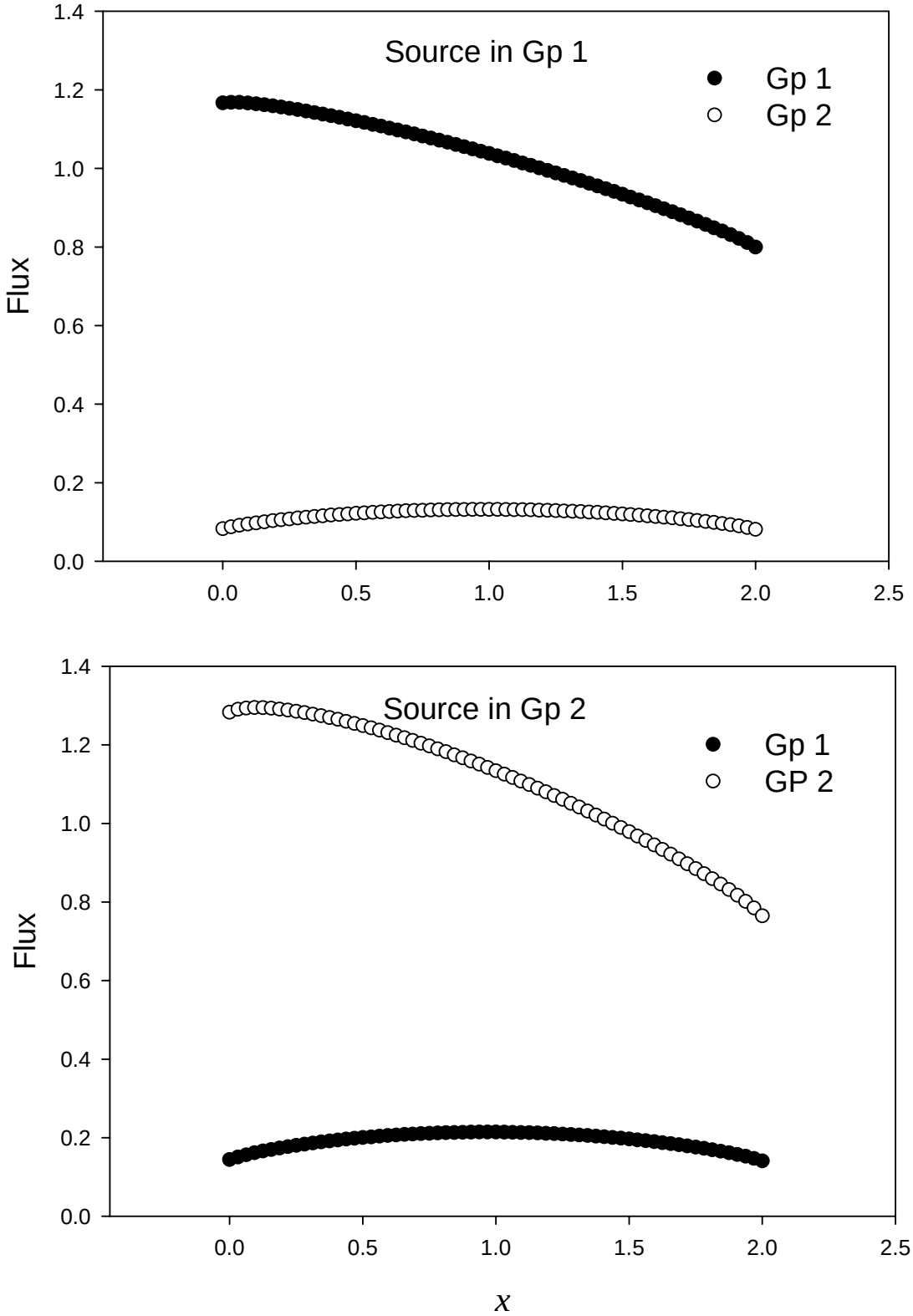

Fig. 5 Two group bare Pu slab of thickness 2 cm

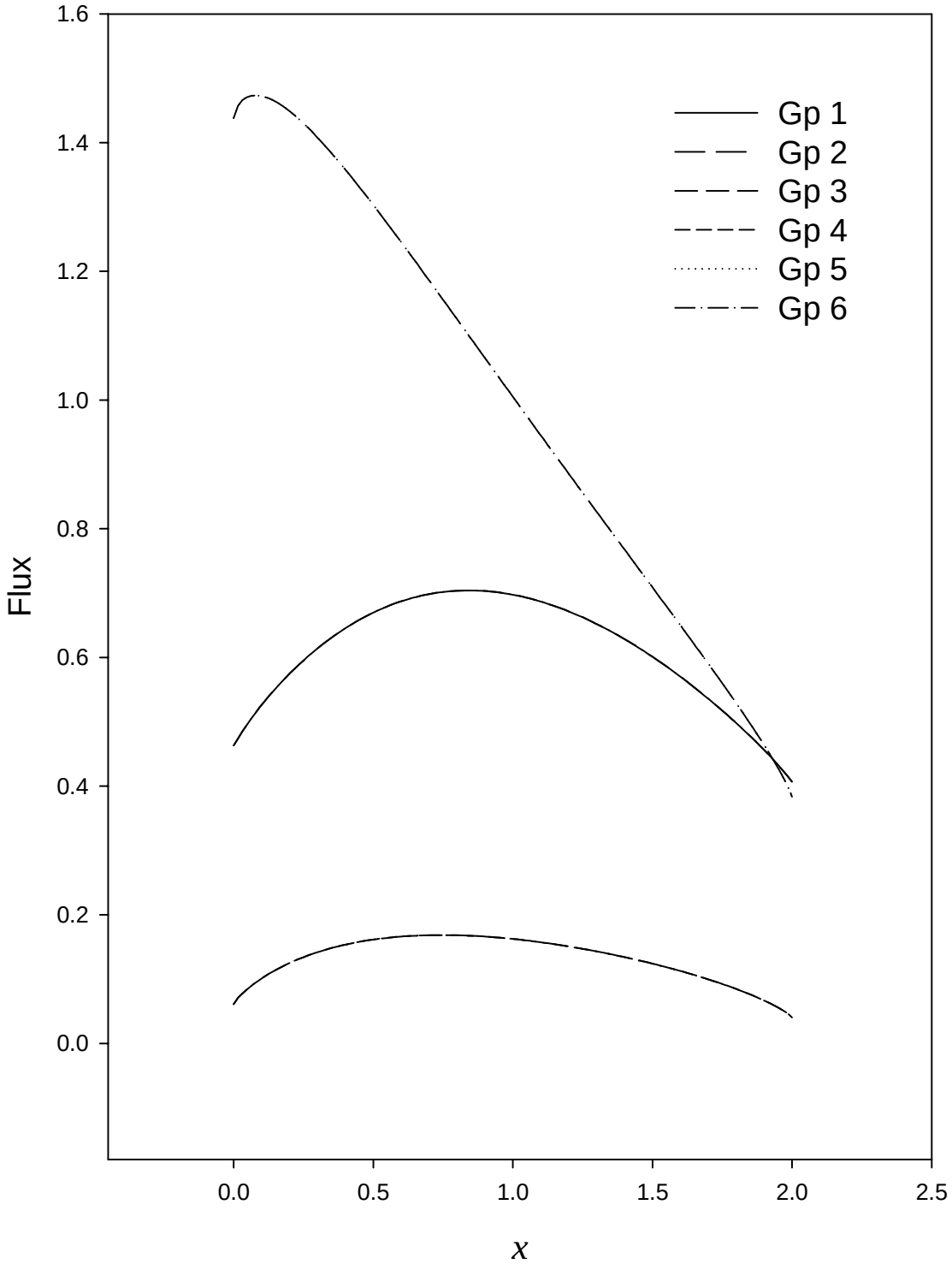

Fig. 6 Six-group calculation with sources in groups 2 and 5

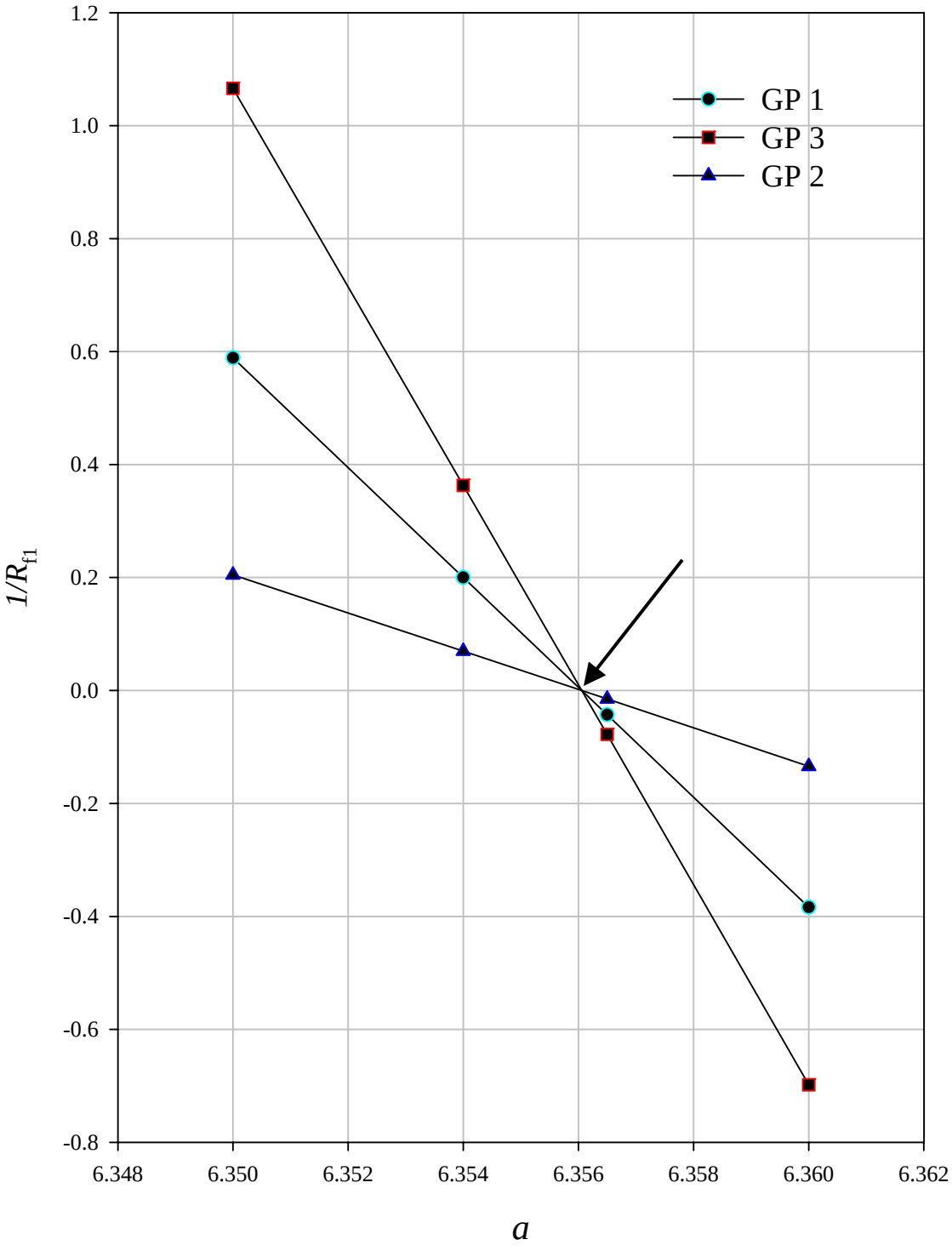

Fig. 7 Approach to criticality for 6-group case

CONCLUDING REMARKS

The original tasking for this grant was the following:

Task 1: 1-D Benchmarks
1.1 One-group Heterogeneous Media
+ single slab
+ heterogeneous slab
1.2 Multigroup Heterogeneous Media
+ single slab
+ heterogeneous slab
1.3 Infinite Media
+ line source
+ shell source
+ solid spherical source

Task 2: Multi-D Benchmarks
2.1 One-group infinite media
+ finite line source
+ partial spherical shell source
2.2 Multigroup infinite media
+ finite line source
+ partial spherical shell source
3.3 Infinite Media general
+ Helical line source demonstration
+ General line source

Essentially, the first task was entirely completed and is reported here. The theory for all of **Task 2** is currently in place and will at a later date be published as archival journal articles. Unfortunately, the duration of the project was not enough to complete **Task 2** in publishable form.

The following conference proceedings originated from this work:

"Multigroup Neutral Particle Transport Theory Revisited: The Development of an Analytical Benchmark," PHYSOR02, Seoul, Korea (2002)

"Analytical Radiation Transport Benchmarks for the Next Century," *Trans. Am. Nucl. Soc.*, **86**, 172-174 (2002)

"An Analytical Multigroup Neutral Particle Transport Benchmark," *Trans. Am. Nucl. Soc.*, **87**, 174-177 (2002)

"A 3-D Source Transport Benchmark," *Trans. Am. Nucl. Soc.*, **87**, 177-180 (2002)